1   **Trans-pacific transport and evolution of aerosols: Evaluation of quasi-**

2   **global WRF-Chem simulation with multiple observations**

3   [1,2]Zhiyuan Hu, [2]Chun Zhao, [1]Jianping Huang, [2]L. Ruby Leung, [2]Yun Qian, [3,4]Hongbin

4   Yu, [5]Lei Huang, [5]Olga V. Kalashnikova

6   [1]Key Laboratory for Semi-Arid Climate Change of the Ministry of Education, Lanzhou

7   University, Gansu, China

8   [2]Atmospheric Sciences and Global Change Division, Pacific Northwest National

9   Laboratory, Richland, WA, USA

10   [3]Earth System Science Interdisciplinary Center, University of Maryland, MD, USA

11   [4]Earth Science Division, NASA Goddard Space Flight Center, MD, USA

12   [5]Jet Propulsion Laboratory, NASA, Pasadena, CA, USA

16   Manuscript for submission to *WRF-Chem special issue in Geosci. Model Dev.*

19   *Corresponding authors:

20   Chun Zhao, phone: (509) 371-6372; email: chun.zhao@pnnl.gov

Abstract

A fully coupled meteorology-chemistry model (WRF-Chem) has been configured to conduct quasi-global simulation for the 5 years of 2010-2014 and evaluated with multiple observation datasets for first time. The evaluation focuses on the simulation over the trans-Pacific transport region using various reanalysis and observational datasets for meteorological fields and aerosol properties. In general, precipitation and winds are well simulated by the model. The simulation captures the overall spatial and seasonal variability of satellite retrieved aerosol optical depth (AOD) and absorbing AOD (AAOD) over the Pacific that is determined by the outflows of pollutants and dust and the emissions of marine aerosols. The assessment of simulated extinction Angstrom exponent (EAE) indicates that the model generally reproduces the variability of aerosol size distributions as seen by satellites. In addition, the vertical profile of aerosol extinction and its seasonality over the Pacific that are dominated by marine aerosols near the surface and the outflow of pollutants and dust above 4 km are also well simulated. The difference between the simulation and satellite retrievals can be mainly attributed to model biases in estimating marine aerosol emissions as well as the satellite sampling and retrieval uncertainties. Compared with the surface measurements over the western U.S., the model reproduces the observed magnitude and seasonality of dust, sulfate, and nitrate surface concentrations, but significantly underestimates the peak surface concentrations of carbonaceous aerosol likely due to model biases in the spatial and temporal variability of biomass burning emissions and secondary organic aerosol (SOA) production. A sensitivity simulation shows that the trans-Pacific transported dust, sulfate, and nitrate can make significant contribution to surface concentrations over the rural areas of the

45   western U.S., while the peaks of carbonaceous aerosol surface concentrations are

46   dominated by the North American emissions. Both the retrievals and simulation show

47   small interannual variability of aerosol characteristics for 2010-2014 averaged over three

48   Pacific sub-regions. The evaluation in this study demonstrates that the WRF-Chem quasi-

49   global simulation can be used for investigating trans-Pacific transport of aerosols and

50   providing reasonable inflow chemical boundaries for the western U.S. to further

51   understand the impact of transported pollutants on the regional air quality and climate

52   with high-resolution nested regional modeling.

1 Introduction

Aerosols, including from natural and anthropogenic sources in Europe, North Africa, and East Asia, can be transported across Pacific Ocean thousands of miles downwind to North America and even beyond. Previous studies using ground-based and satellite measurements and numerical models estimated about 7-10 days of travel time for aerosols to traverse the Pacific Ocean (Eguchi et al., 2009). These transported aerosols can play an important role in atmospheric composition (Yu et al., 2008), air quality (Jaffe et al., 1999; VanCuren, 2003; Heald et al., 2006; Chin et al., 2007; Fischer et al., 2009; Yu et al., 2012; Tao et al., 2016), and regional weather and climate (Eguchi et al., 2009; Yu et al., 2012; Creamean et al., 2013; Fan et al., 2014) over the U.S. West Coast. At the surface, Heald et al. (2006) found that Asian anthropogenic aerosol plume increased aerosol concentration in elevated regions of the northwestern U.S. by 0.16 μg m^{-3} in spring 2001. Chin et al. (2007) also found that long-range transported dust increased the annual mean fine particle concentrations by 0.5-0.8 μg m^{-3} over the western U.S., with a maximum enhancement in spring. The trans-Pacific transported aerosols can also significantly absorb and scatter solar radiation (Yu et al., 2012; Fast et al., 2014; Tao et al., 2016), and serve as cloud condensation nuclei and ice nuclei that affect winter storms in the western U.S. (Sassen, 2002; Ault et al., 2011; Creamean et al., 2013; Fan et al., 2014). Deposition of the transported aerosols on snowpack in elevated regions (Hadley et al., 2010) may also accelerate snowmelt and influence the regional hydrological cycle and climate over the western U.S. (Qian et al., 2009 and 2015; Painter et al., 2010). Hence it is important to quantify the trans-Pacific transport of aerosols and how they evolve over the long distance.

78   Previous studies have used global models to quantify the long-range transport of

79   aerosols to the western U.S. (Fairlie et al., 2007; Heald et al., 2006; Chin et al., 2007;

80   Hadley et al., 2007). However, simulations were performed at relatively coarse

81   resolutions (typically 1-2 degrees) that cannot fully resolve the large geographical

82   variability of aerosols over the western U.S. with complex topography (Zhao et al.,

83   2013a). Coarse resolution simulations also lack the capability to fully resolve aerosol-

84   cloud-precipitation interaction. Some studies have reported regional simulations at

85   relatively high resolutions over the western U.S. (e.g., Zhao et al., 2013a; Fan et al.,

86   2014; Fast et al., 2014). However, most of them either used sparse in-situ observations to

87   provide lateral boundary conditions that are only suitable for idealized or short-term

88   sensitivity studies, or used simulations from global models with inconsistent physics and

89   chemistry schemes to provide lateral boundary conditions, which introduce biases in

90   estimating the contribution and effect of trans-Pacific transported aerosols.

91   To investigate the impact of trans-Pacific transported aerosols on regional air

92   quality and climate of the US West Coast, a multi-scale modeling framework including

93   global simulation at coarse resolutions that captures the large-scale circulation and

94   provide consistent chemical lateral boundaries for nested regional simulation at high

95   resolutions is needed. WRF-Chem, the Weather Research and Forecasting (WRF) model

96   (Skamarock et al., 2008) coupled with a chemistry component (Grell et al., 2005), is such

97   a modeling framework. As a state-of-the-art model, WRF-Chem supports nested

98   simulations, and includes complex aerosol processes and interactions between aerosols

99   and radiation, clouds, and snow albedo (Zhao et al., 2014). The model has been used

100   extensively to study aerosols and their impacts on air quality and climate at regional

101   scales (e.g., Fast et al., 2006, 2009; Gustafson et al., 2007; Qian et al., 2010; Gao et al.,

102   2011, 2014; Shrivastava et al., 2011; Chen et al., 2013, 2014; Zhao et al., 2010, 2011,

103   2012, 2013a; 2014). Zhao et al. (2013b) is the first study to use WRF-Chem for quasi-

104   global (180° W-180° E, 60° S-70° N) simulations at a resolution of 1° × 1° to examine

105   uncertainties in simulating global dust mass balance and radiative forcing.

106   Although the quasi-global WRF-Chem simulation described by Zhao et al. (2013b)

107   has been used to provide realistic chemical lateral boundary conditions for multiple

108   regional modeling studies (e.g., Zhao et al., 2014; Fan et al., 2015), its evaluation has not

109   been documented so far. In this study, the WRF-Chem simulation for 2010-2014 is

110   evaluated extensively using observational data. For lack of in-situ observations over East

111   Asia and Pacific Ocean during the simulation period, evaluation is performed mainly

112   using reanalysis and satellite retrieval (e.g., CALISPO, MODIS, and MISR) datasets,

113   along with some available ground-based observations from AERONET and IMPROVE

114   in the region. We focus on the simulation over the trans-Pacific transport region as a first

115   step to evaluate the simulation for providing consistent lateral chemical boundaries for

116   nested regional simulations used to investigate the impact of transported aerosols on

117   regional air quality and climate. Spatial evolution of aerosols during the trans-Pacific

118   transport as well as their seasonal and annual variability simulated by WRF-Chem will

119   also be characterized.

120   In the following sections, the detailed setup of WRF-Chem will be described in

121   Section 2. In Section 3 ground-based measurements and satellite retrievals will be

122   presented. In Section 4, we evaluate the WRF-Chem simulated spatial distributions and

123   seasonal and annual variability of aerosols across the Pacific with the observations. The

124   conclusion can be found in Section 5.

125

126   **2 Model description**

127   In this study, WRF-Chem (3.5.1), updated by scientists at Pacific Northwest

128   National Laboratory (PNNL), is used and briefly described in Section 2.1. Section 2.2

129   discusses the setup of model simulations for this study. In Section 2.3, the emissions used

130   in the simulations are described, including anthropogenic and biomass burning emissions,

131   and mineral dust and sea-salt emissions.

132   **2.1 WRF-Chem**

133   The MOSAIC (Model for Simulation Aerosol Interactions and Chemistry) aerosol

134   module (Zaveri et al., 2008) coupled with the CBM-Z (carbon bond mechanism)

135   photochemical mechanism (Zaveri and Peters, 1999) in WRF-Chem is selected in this

136   study. MOSAIC uses a sectional approach to represent aerosol size distributions with

137   four or eight discrete size bins in the current version of WRF-Chem (Fast et al., 2006).

138   All major aerosol components including sulfate (SO_4^{-2}), nitrate (NO_3^-), ammonium (NH_4^+),

139   black carbon (BC), organic matter (OM), sea-salt, and mineral dust are simulated in the

140   model. The MOSAIC aerosol scheme includes physical and chemical processes of

141   nucleation, condensation, coagulation, aqueous phase chemistry, and water uptake by

142   aerosols. Dry deposition of aerosol mass and number is simulated following the approach

143   of Binkowski and Shankar (1995), which includes both turbulent diffusion and

144   gravitational settling. Wet removal of aerosols by grid-resolved stratiform clouds and

145   precipitation includes in-cloud removal (rainout) and below-cloud removal (washout) by

146   impaction and interception, following Easter et al. (2004) and Chapman et al. (2009).

147   Cloud-ice-borne aerosols are not explicitly treated in the model, but the removal of

148   aerosols by the droplet freezing process is considered. Convective transport and wet

149   removal of aerosols by cumulus clouds follow Zhao et al. (2013b).

150   Aerosol optical properties such as extinction, single scattering albedo (SSA), and

151   asymmetry factor for scattering are computed as a function of wavelength for each model

152   grid box. Aerosols are assumed internally mixed in each bin (i.e., a complex refractive

153   index is calculated by volume averaging for each bin for each chemical constituent of

154   aerosols). The Optical Properties of Aerosols and Clouds (OPAC) data set (Hess et al.,

155   1998) is used for the shortwave (SW) and longwave (LW) refractive indices of aerosols,

156   except that a constant value of 1.53+0.003i is used for the SW refractive index of dust

157   following Zhao et al. (2010, 2011). A detailed description of the computation of aerosol

158   optical properties in WRF-Chem can be found in Fast et al. (2006) and Barnard et al.

159   (2010). Aerosol radiative feedback is coupled with the Rapid Radiative Transfer Model

160   (RRTMG) (Mlawer et al., 1997; Iacono et al., 2000) for both SW and LW radiation as

161   implemented by Zhao et al. (2011). The optical properties and direct radiative forcing of

162   individual aerosol species in the atmosphere are diagnosed following the methodology

163   described in Zhao et al. (2013a). Aerosol-cloud interactions were included in the model

164   by Gustafson et al. (2007) for calculating the activation and resuspension between dry

165   aerosols and cloud droplets.

166   **2.2 Numerical experiments**

167   Following Zhao et al. (2013b), we use a quasi-global channel configuration with

168   periodic boundary conditions in the zonal direction and 360 × 145 grid cells (180° W-180°

169   E, 67.5° S-77.5° N) to perform simulation at 1° horizontal resolution over the period of

170   2010-2014. This circumvents some technical difficulties in running global WRF-Chem in

171   v3.5.1 for a near global coverage to characterize the trans-Pacific transport of aerosols.

172   The simulation is configured with 35 vertical layers up to 50 hPa. The meteorological

173   initial and lateral meridional boundary conditions are derived from the National Center

174   for Environmental Prediction final analysis (NCEP/FNL) data at 1° horizontal resolution

175   and 6 h temporal intervals. The modeled wind components u and v and atmospheric

176   temperature are nudged towards the NCEP/FNL reanalysis data throughout the domain

177   with a nudging timescale of 6 h in all cases (Stauffer and Seaman, 1990). This provides a

178   more realistic simulation of large-scale circulation, which is important for modeling long-

179   range transport. The chemical initial and meridional boundary conditions are taken from

180   the default profiles in WRF-Chem, which are the same as those used by McKeen et al.

181   (2002) and are based on averages of mid-latitude aircraft profiles from several field

182   studies over the eastern Pacific Ocean. The impact of chemical boundary conditions on

183   the simulated results is negligible (Zhao et al. 2013b). This study uses a set of selected

184   schemes for model physics, including the MYJ (Mellor–Yamada–Janjic) planetary

185   boundary layer scheme, Noah land surface scheme, Morrison 2-moment microphysics

186   scheme, Kain-Fritsch cumulus scheme, and RRTMG longwave and shortwave radiation

187   schemes.

188   **2.3 Emissions**

189   Anthropogenic emissions are obtained from the REanalysis of the TROpospheric

190   (RETRO) chemical composition inventories (http://retro.enes.org/index.shtml) except

191   over East Asia and the United States. Over the U.S., the National Emission Inventory

192   (NEI) 2005 (WRF-Chem user guide from http://ruc.noaa.gov/wrf/WG11/Users_guide.pdf)

193   is used. Over East Asia, the Asian emission inventory described by Zhang et al. (2009) at

194   0.5°x0.5° horizontal resolution for 2006 is used except that BC, OC, and sulfate

195   emissions over China are from the China emission inventory for 2010 described by Lu et

196   al. (2011) at a 0.1°x0.1° horizontal spatial resolution and a monthly temporal resolution

197   for the simulation period. Biomass burning emissions are obtained from the Global Fire

198   Emissions Database, Version 3 (GFEDv3) with monthly temporal resolution (van der

199   Werf et al., 2010) and vertically distributed following the injection heights suggested by

200   Dentener et al. (2006) for the Aerosol Comparison between Observations and Models

201   (AeroCom) project. Sea-salt emission follows Zhao et al. (2013a), which is based on

202   Gong (2003) to include correction of particles with radius less than 0.2 μm and Jaegle et

203   al. (2011) to include the sea-salt emission dependence on sea surface temperature.

204   Vertical dust emission fluxes are calculated with the Goddard Chemical Aerosol

205   Radiation Transport (GOCART) dust emission scheme (Ginoux et al., 2001), and the

206   emitted dust particles are distributed into the MOSAIC aerosol size bins following a

207   theoretical expression based on the physics of scale-invariant fragmentation of brittle

208   materials derived by Kok (2011). For MOSAIC 8-bin, dust particles are emitted into

209   eight size bins with mass fractions of 10^{-6}%, 10^{-4}%, 0.02%, 0.2%, 1.5%, 6%, 26%, and

210   45%, respectively. Although the main purpose of this study is to evaluate the WRF-Chem

211   simulations, a sensitivity simulation, in which dust, fire, and anthropogenic emissions

212   over North America (10°N-70°N and 170°W-60°W) are removed, is also conducted to

213   understand the contribution of trans-Pacific transported aerosols to the surface aerosol

214   concentrations over the western U.S.

215

3 Aerosol Observations

3.1 Satellite Retrievals

3.1.1 MODIS

The Moderate Resolution Imaging Spectroradiometer (MODIS) instrument onboard the NASA EOS Terra satellite observes Earth in 36 spectral bands from 0.4 to 14.4 μm, and provides nearly daily global coverage with local equatorial overpass time of about 10:30 am since 2000 (King et al., 1999). The "dark target" algorithm has been developed to retrieve AOD and size parameters (Angstrom exponent, effective radius, and fine-mode fraction) over waters and vegetated lands (Kaufman et al., 1997; Remer et al., 2005). The "deep blue" algorithm has been implemented to retrieve AOD over bright land initially, which then has also been extended to vegetated land (Hsu et al., 2006, 2013). MODIS aerosol products have been widely used to characterize the regional, seasonal, and global distribution of aerosol and its components (Yu et al., 2003, 2009; Chin et al., 2004; Kaufman et al., 2005a), estimate aerosol radiative forcing (Yu et al., 2004; Remer and Kaufman, 2006), and study aerosol-cloud interactions (Kaufman et al., 2005b; Koren et al., 2005; Yu et al., 2007). In this study, MODIS data from the collection 5.1 are used. We use the "deep blue" AOD over land and the "dark target" AOD over ocean, both at 550 nm and at 1° x 1° horizontal resolution. Also, we use the "dark target" over-ocean extinction Angstrom exponent (EAE) over the 470-660 nm wavelength range to evaluate model simulations of particle size information (Anderson et al., 2005; Remer et al., 2005; Levy et al., 2013).

3.1.2 MISR

238   The Multi-angle Imaging SpectroRadiometer (MISR) instrument onboard the

239   Terra spacecraft crosses the equator at ~10:30 AM local time since 1999. It observes

240   continuously in four narrow spectral bands centered at 446, 558, 672 and 866 nm using

241   nine separate cameras oriented along the orbital track with surface viewing zenith angles

242   ranging from $\pm70.5°$ (Diner et al., 1998). Aerosol retrievals are performed on 16×16

243   patches of 1.1 km sub-regions, yielding an aerosol product at 17.6×17.6 km spatial

244   resolution, referred to as a "Level 2" product (Martonchik et al., 2002). MISR Level 2

245   aerosol products have been described in Kahn et al (2009). The latest version (Version 22)

246   of MISR aerosol product also provides the fraction of AOD due to "fine" (particle radii

247   <0.35 μm), "medium" (particle radii between 0.35 and 0.7 μm) and "large" (particle

248   radii >0.7 μm) particles as well as the fraction of AOD due to "spherical" and

249   "nonspherical" particles at the four MISR spectral bands. Here, we compare the MISR

250   AOD at 550 nm from Version 22 of Level 2 with the model results.

251   **3.1.3 OMI**

252   OMI onboard the NASA Aura satellite has a daily global coverage, and crosses

253   the equator at 1:45 PM local time. The nadir horizontal resolution of OMI is 24×13 km^2.

254   In this study the OMAERUV Level 2 Collection 003 V1.4.2 product (Jethva et al., 2014)

255   is used as an independent data set providing SSA that is derived based on the reflectances

256   measured by the OMI instrument at 0.39 μm. The information on aerosol absorption in

257   OMI measurements comes, to a large extent, from the interaction with Rayleigh

258   scattering in the UV spectral region (Torres et al., 2013). The retrieved parameters are

259   also reported at 0.38 μm and 0.50 μm. Current OMI AOD has positive biases likely due

260   to a combination of factors including cloud contamination, surface albedo effects,

261   radiometric calibrations, and misidentified aerosol type (Ahn et al., 2008). Therefore, in

262   this study, OMI AAOD at 500 nm is reconstructed using the WRF-Chem simulated 500

263   nm AOD and OMI SSA at 500 nm with the formula of $AAOD_{OMI}=AOD_{MODEL}\times(1-$

264     $SSA_{OMI})$.

265   **3.1.4 CALIPSO**

266   In this study, we use aerosol extinction profiles retrieved by the Cloud-Aerosol

267   Lidar with Orthogonal Polarization (CALIOP) onboard the Cloud-Aerosol Lidar and

268   Infrared Pathfinder Satellite Observation (CALIPSO) satellite. The CALIPSO satellite

269   was launched into a Sun-synchronous orbit on 28 April 2006. CALIOP is a dual-

270   wavelength polarization lidar and is designed to acquire vertical profiles of attenuated

271   backscatter from a near nadir-viewing geometry during both day and night phase (Winker

272   et al., 2007). In this study, the aerosol extinction profiles at a nominal horizontal

273   resolution of 5 km from the CALIPSO Level 2 profile products are used to evaluate the

274   model. We focus on the CALIOP nighttime observations in cloud-free condition, because

275   nighttime observations have higher accuracy than daytime observations (Winker et al.,

276   2009).

277   The cloud-aerosol discrimination (CAD) score, which is an indicator that

278   measures confidence level of the discrimination between clouds (positive value) and

279   aerosols (negative value), is used to help screen out aerosol profiles that contain cloud

280   signals. We include the aerosol data with CAD score between -20 and -100, the same as

281   Yu et al., (2010, 2015). The other screening is to exclude aerosol layers where the

282   retrieval algorithm has to adjust the initially selected lidar ratio that is based on the type

283   and subtype of the aerosol layer to be analyzed. It should be noted that when the aerosol

284   extinction is not detected by CALIOP, we set its value and also the corresponding model

285   result equal to zero, and then we compare CALIOP extinction profiles with the model

286   and analyze the seasonal variation.

287   **3.2 Ground-based observations**

288   **3.2.1 AERONET**

289   The AErosol RObotic NETwork (AERONET) is a globally distributed remote

290   sensing network for aerosol monitoring from ground stations (Holben et al., 1998).

291   AERONET uses the Cimel sun/sky photometer that measures AOD in 16 spectral

292   channels (340-1640 nm). The measurements provide products every 15 minutes during

293   daytime. In addition, an inversion algorithm is used for the retrieval of aerosol size

294   distribution, complex refractive index, single-scattering albedo, and phase function

295   (Dubovik and King, 2000; Dubovik et al., 2002). The spectral AOD from AERONET has

296   an accuracy of ±0.01 (Eck et al., 1999; Holben et al., 2001). In the analysis presented in

297   this paper, the cloud screened and quality assured level 2.0 products are used. AERONET

298   products do not measure at wavelength 0.55 μm, so we calculate them through using the

299   Angstrom exponent and the values at two nearest wavelengths 0.5 μm and 0.675 μm. The

300   AERONET sites are located along the trans-Pacific transport pathways, so the products

301   are important for evaluating the model results. Five sites over East Asia, one island site

302   over North Pacific, and four sites over the western U.S. are selected for comparison as

303   shown in Figure 1.

304   **3.2.2 IMPROVE**

305   The Interagency Monitoring for Protected Visual Environments (IMPROVE)

306   network was initiated in 1985 by U.S. federal agencies including EPA, National Park

307   Services, Department of Agriculture-Forest Service, and other land management agencies

308   as a part of the EPA Regional Haze program (Malm et al., 1994). The network monitors

309   the visibility conditions and changes in national parks and wilderness areas on a long-

310   term basis. The detail sample collection and analytical methodology have been given by

311   Hand   et   al.,   (2011),   and   the   data   can   be   downloaded   from

312   (http://views.cira.colostate.edu/fed/DataWizard/Default.aspx). There are 15 sites (Fig. 1)

313   along the west coast selected to compare with the surface aerosols of the model. In this

314   study, the mass concentrations of sulfate, nitrate, EC, OC, and dust in $PM_{2.5}$ (particulate

315   matter with aerodynamic diameter less than 2.5 μm) are used to evaluate the model. The

316   fine dust was calculated following the formula (Malm et al., 1994; Zhao et al., 2013a):

317   $$PM_{2.5}\text{-Dust} = 2.2[Al] + 2.49[Si] + 1.63[Ca] + 2.42[Fe] + 1.94[Ti]$$

318   Where [Al], [Si], [Ca], [Fe], and [Ti] represent the mass concentration of aluminum,

319   silicon, calcium, iron, and titanium, respectively.

320

321   **4 Results**

322   **4.1 Wind fields and precipitation**

323   Winds and precipitation are two crucial meteorological factors playing important

324   roles in aerosol emission, transport, and removal. The seasonal mean wind fields at 850

325   hPa averaged for the period of 2010-2014 from the WRF-Chem simulation are compared

326   with the Modern-Era Retrospective analysis for Research and Applications (MERRA)

327   reanalysis data (Rienecker et al., 2011) (Figure 2). Strong westerly winds occur over the

328   North Pacific throughout the seasons with a peak (up to 12 m/s) in boreal winter (DJF)

329   followed by boreal spring (MAM). In general, the model can well reproduce the spatial

330   pattern of winds across the Pacific and its seasonality. Figure 3 shows the spatial

331   distribution of seasonal mean precipitation from the Global Precipitation Climatology

332   Project (GPCP) observation (Huffman et al., 2001) and WRF-Chem simulation averaged

333   for the period of 2010-2014. Over East Asia, precipitation reaches a maximum during the

334   boreal summer (JJA) followed by MAM. In the North Pacific basin, the largest

335   precipitation occurs in DJF along the storm tracks with the maximum westerlies. Over the

336   U.S. west coast, precipitation peaks during DJF and reaches a minimum in JJA. The

337   simulation reasonably reproduces the spatial and seasonal variation of precipitation, with

338   overestimation in some regions, particularly over the Inter-Tropical Convergence Zone

339   (ITCZ) and western tropical Pacific that are south of the major pathway of trans-Pacific

340   transport.

341

342   **4.2 Aerosol optical depth**

343   4.2.1 Spatial and temporal variation

344   Figure 4 shows the spatial distributions of seasonal mean AOD at 550 nm across

345   the Pacific from Asia to North America averaged for 2010-2014 from the retrievals of

346   MODIS and MISR onboard Terra and the corresponding WRF-Chem simulation. In order

347   to reduce the sampling discrepancy between the two retrievals, the daily results from the

348   two satellite retrievals and simulation are sampled and averaged at the same time and

349   location. This way of averaging leads to the blank areas of missing values, which are

350   relatively large in JJA. Satellite retrievals show that AOD is high over the Asian

351   continent and gradually decreases across the Pacific. High AOD coincides with the sub-

352   tropical jet (30°N-50°N, Fig. 2) over the Pacific and results from wind-induced increase

353   in sea-salt loading and the Asian pollutant outflow. Seasonal variation of aerosols across

354   the Pacific is evident, with peak AOD over the western Pacific in MAM and minimum

355   AOD in JJA and SON. Previous studies found that trans-Pacific transport of air pollutants

356   is most efficient in MAM due to active cyclonic activity and that pollutants are lifted to

357   the free troposphere where it can be rapidly transported across the Pacific by strong

358   westerlies (e.g., Forster et al., 2004; Liang et al., 2004; Heald et al., 2006; Yu et al., 2008).

359   The WRF-Chem simulation generally well captures the observed spatial and seasonal

360   variability of AOD across the Pacific. The model underestimates the oceanic AOD to the

361   south of 20^oN, which may be due to underestimation of marine emissions and/or

362   overestimation of aerosol wet removal associated with the positive bias in precipitation.

363   The discrepancy may also be due to cloud contamination in the retrievals that leads to an

364   overestimation of AOD in some regions of North Pacific (e.g., Zhang and Reid, 2006).

365   The model also simulates lower AOD over the continent of North America compared

366   with satellite retrievals. The difference between the simulation and retrievals may be due

367   to the uncertainty in satellite retrievals over the continents (e.g., Liu et al., 2004; Levy et

368   al., 2010).

369   Since this study focuses on the trans-Pacific transport and evolution of aerosols,

370   the Pacific is further divided into three sub-regions (Region 1: 20°N-50°N and 120°E-

371   140°E; Region 2: 20°N-50°N and 140°E-140°W; Region 3: 20°N-50°N and 140°W-

372   120°W) representing the West Pacific, the Central Pacific, and the East Pacific shown as

373   the black boxes in Figure 4 for analysis. Figure 5 shows the seasonal mean 550 nm AOD

374   over the three sub-regions from the MISR and MODIS retrievals and the corresponding

375   WRF-Chem simulation at the pass time of MISR and MODIS, respectively, averaged for

376   2010-2014. It shows clearly that AOD peaks in MAM in all the regions across the Pacific.

377   The simulation successfully reproduces the observed seasonal variability. In general, the

378   MODIS and MISR retrievals are consistent and show that AOD reduces from West

379   Pacific to East Pacific, which is also indicated by the simulation. The interannual

380   variability of AOD over the three sub-regions is small for 2010-2014 indicated by the

381   retrievals and simulation (not shown).

382   Available observations from several AERONET sites (Fig. 1) over East Asia, the

383   Pacific, and western US are also compared with the model simulation. Figure 6 shows the

384   comparison of observed and simulated AOD at three representative AERONET sites for

385   2010-2014 over East Asia, an island of Pacific, and the western US coast. The

386   observations and simulation agree well at all three sites, and both reflect the AOD

387   gradient from East Asia to the western U.S. as shown in Figure 4. Observed AOD is the

388   highest with a mean value of 0.31 at the SACOL site over East Asia and reduces to 0.075

389   at the Midway_Island site, and 0.045 at the Frenchman_Flat site. The model reproduces

390   these values at the three sites with correlation coefficients of 0.45, 0.75, and 0.63,

391   respectively. About 90% of simulated AOD is within a factor of 2 of the AERONET

392   measurements.

393   Figure 7 further shows the monthly variation of AOD averaged at the AERONET

394   sites over East Asia, the Pacific island, and the West US (as shown in Fig. 1) from the

395   AERONET observations, MODIS and MISR retrievals, and WRF-Chem simulation. For

396   the simulated AOD, contributions by dust, BC, OC, sulfate, and other aerosols are also

397   shown. Over East Asia, the MISR and AERONET retrievals agree well in monthly

398   variation. The MODIS retrievals generally overestimate AOD. The simulation reproduces

399   the AERONET observed AOD variability. Model results show that anthropogenic

400   aerosols dominate the AOD from summer to winter while dust can significantly

401   contribute to the AOD in spring. Over the island of Pacific (the Midway_Island site),

402   retrievals from AERONET, MODIS, and MISR are consistent with each other and with

403   the simulation on monthly variation of AOD, primarily determined by the sea-salt aerosol,

404   which shows a minimum in summer months. The trans-Pacific transported aerosols (other

405   than sea-salt) also show strong monthly variation with a maximum in April and a

406   minimum in July. Over the western U.S., both retrievals and simulation show the largest

407   AOD occurs in the spring months, which has significant contribution from the dust

408   aerosol transported across the Pacific (to be discussed in section 4.5). MODIS retrieved

409   lower AOD than MISR, and both retrievals are significantly higher than that from the

410   AERONET retrieval in March-October, while the simulation is more consistent with the

411   AERONET retrievals, which suggests that the difference between the MODIS and MISR

412   retrievals and the simulation over the western US shown in Fig. 4 is due to uncertainty in

413   satellite retrievals.

414

415   4.2.2 Wavelength dependence

416   The wavelength dependence of AOD that can be represented by the extinction

417   Angstrom exponent (EAE) is an indicator of aerosol particle size (Angstrom, 1929;

418   Schuster et al., 2006). In general, relatively small values of EAE indicate that aerosol size

419   distributions are dominated by coarse aerosols typically associated with dust and sea-salt,

420   while relatively large values of EAE indicate fine aerosols usually contributed by

421   anthropogenic pollution and biomass burning. Figure 8 shows the seasonal mean EAE

422   averaged for 2010-2014 from the MODIS retrievals and the WRF-Chem simulation over

423   the three sub-regions. The retrievals show clearly that the EAE values peak in JJA and

424   reach a minimum in DJF in all three sub-regions. This seasonality reflects the fact that

425   photochemistry is most active in JJA to produce fine aerosol particles such as sulfate. In

426   general, the simulation successfully reproduces the observed EAE seasonality. The

427   retrievals and simulation also show that the values of EAE are greater in the West Pacific

428   than in the Central and East Pacific. This pattern may reflect the dominance of the Asian

429   pollutant outflow on the aerosol size distributions over the West Pacific, while the

430   relatively large-size particles of sea-salt dominates in the other two regions. Again, the

431   annual variability of EAE over the three sub-regions is small (not shown).

432

433   **4.3 Aerosol absorption optical depth**

434   Light absorbing aerosols such as BC and dust play an important role in the

435   atmosphere to absorb radiation and change the heating profiles in the atmosphere.

436   Aerosol absorption optical depth (AAOD) is an important parameter for evaluating the

437   model performance in simulating light absorbing aerosols. Figure 9 shows the seasonal

438   mean AAOD at 500 nm averaged for 2010-2014 and over the three sub-regions from the

439   OMI retrievals and the WRF-Chem simulation. Both retrievals and simulation show

440   small interannual variability (not shown). Both the retrievals and simulation show that

441   AAOD peaks in MAM followed by JJA over the three sub-regions, which may be due to

442   the stronger outflow of dust and anthropogenic pollutants in the two seasons. The

443   simulated AAOD over West Pacific agrees reasonably well with the OMI retrieval in DJF

444   but is higher in the other three seasons. Over Central Pacific, the simulation generally

445   reproduces the retrieved AAOD, except overestimating (underestimating) the retrieved

446   values in JJA (DJF). Over East Pacific, the simulated AAOD is consistent with the

447   retrieved values with some overestimation in JJA. The retrievals and simulation show

448   large variability of AAOD, and they generally agree within the 10th and 90th percentiles

449   of each other. AAOD is larger over West Pacific than Central and East Pacific, which is

450   consistent with the AOD pattern.

451   The AERONET retrieval products (version 2) also provide AAOD values but

452   only at the sites and time when the total AOD exceeds a threshold value of 0.4 at 440 nm

453   because the AERONET inversion algorithms require a high signal-to-noise ratio to

454   retrieve some optical products such as AAOD. The total AOD values over Central Pacific

455   and the western US are less than this threshold value most of the time, and only AAOD

456   values retrieved at the East Asian sites are available and reliable. Figure 10 shows the

457   monthly variation of AAOD averaged at the AERONET sites over East Asia (Fig. 1)

458   from the AERONET observations, OMI retrievals, and WRF-Chem simulation. The

459   AERONET retrievals show the monthly variation of AAOD over East Asia with

460   relatively lower values in JJA probably due to wet removal of aerosols by precipitation

461   and mixing with clean marine air during the East Asian summer monsoon (Zhao et al.,

462   2010). The simulation generally captures the observed monthly variability, but

463   overestimate AAOD in the warm months such as August and September. The model

464   shows that AAOD over East Asia is dominated by BC and is partly contributed by dust.

465   Other aerosols contribute to small amount of AAOD due to the internal mixing of

466   aerosols in the atmosphere (Zhao et al., 2013a). The model positive biases in AAOD in

467   the warm months may be partly related to the constant anthropogenic BC emissions

468   applied throughout the seasons while previous studies showed that anthropogenic BC

469   emissions may have seasonal variation with lower values in the warm months (Lu et al.,

470   2010).

471   It is noteworthy that the OMI retrieved AAOD is lower than that from AERONET

472   and WRF-Chem, particularly in JJA and SON. The lower OMI AAOD may indicate

473   positive biases in the OMI SSA retrievals over East Asia and West Pacific (Fig. 9) that is

474   significantly affected by the East Asian outflow. The difference between the simulation

475   and OMI retrievals over East Pacific may be partly due to negative biases in modeling

476   SSA; however, it is noteworthy that the OMI retrievals may have difficulty in

477   distinguishing the ocean color effects from those of low aerosol concentrations in the UV

478   spectral range and ignoring less-sufficient amounts of absorbing aerosols [Veihelmann et

479   al., 2007; Torres et al., 2013]. In addition, the OMI retrievals may also have cloud

480   contamination issue because of the large footprint.

481

4.4 Aerosol vertical distributions

483   Column integrated properties of aerosol (e.g., AOD and AAOD) provide useful

484   information in regard to atmospheric aerosol loading but little information on the vertical

485   distribution of aerosols. Previous studies found that simulated aerosol vertical

486   distributions differ significantly, which can affect the assessments of aerosol impacts on

487   climate and air quality (e.g., Schulz et al., 2006; Textor et al., 2006). CALIPSO with the

488   unique capability provides an opportunity to assess model simulation of aerosol vertical

489   distributions (e.g., Huang et al., 2013). Figure 11 shows the vertical distributions of

490   annual mean aerosol extinction coefficients for 2010-2014 averaged over the three sub-

491   regions from the CALIPSO retrievals and the corresponding WRF-Chem simulation

492   under cloud-free condition. The CALIPSO retrievals show clearly that aerosol extinction

493   coefficients peak near several hundred meters above the surface and then decrease with

494   the altitude over the three sub-regions. The extinction coefficients reduce from West to

495   East Pacific. The model generally reproduces the aerosol extinction vertical distributions.

496   The simulated mass fraction of each aerosol component (Fig. 12) show that below 1 km,

497   sea-salt dominates the total aerosol mass over Central and East Pacific, while the outflow

498   of anthropogenic aerosols and dust also make significant contributions over West Pacific.

499   Above 4 km, dust is the dominant aerosol over all three sub-regions. The simulation is a

500   little higher than the retrievals in the free troposphere (e.g., >4 km) and at the surface. In

501   the free troposphere, the difference may be due to the reduced sensitivity of CALIOP to

502   tenuous aerosol layers above 4 km. At the surface, the lower CALIPSO aerosol extinction

503   may result from a misclassification of polluted continental aerosol as marine aerosol

504   when pollution outflow occurs near the surface and surface contamination during the

505   retrievals (Yu et al., 2010). The model consistently underestimates the aerosol extinction

506   coefficients between surface and 1 km in all three sub-regions, which may indicate that

507   the model has negative biases for estimating marine aerosol emissions, as shown in Fig. 4.

508   The seasonal variation of aerosol extinction profiles averaged for 2010-2014 (Fig.

509   13) shows the spring maximum, particularly above 2 km, over all three sub-regions from

510   both the CALIPSO retrievals and the model simulation. This is likely due to the

511   seasonality of dust outflow over the Pacific (Fig. 14) that dominates the aerosol masses

512   above 2 km with a peak in spring (e.g., Huang et al. 2013). Over West Pacific, the model

513   reasonably reproduces the retrieved aerosol extinction profiles through the seasons with a

514   relatively larger negative bias below 1 km in DJF, when sea-salt has a relatively larger

515   contribution near the surface (Fig. 14). In JJA, similar amount of aerosols as that in

516   MAM has the largest contribution from the anthropogenic pollutant outflow among the

517   seasons with a peak at ~ 2 km above the surface. Over Central and East Pacific, the

518   model also well captures the vertical distributions with a relatively larger negative bias

519   below 1 km in DJF. Over these two regions, the seasonality of the vertical shape of each

520   aerosol component contribution is similar to that over West Pacific, except that the sea-

521   salt contribution is larger near the surface (Fig. 14).

522

523   **4.5 Aerosol surface mass concentrations over the West US**

524   For lack of in-situ observations of aerosol masses over the Pacific, measurements

525   of surface fine aerosol ($PM_{2.5}$) component mass concentrations from the IMPROVE

526   network over the western U.S. were widely used for model evaluation of trans-Pacific

527   transport (e.g., Chin et al., 2007; Hadley et al., 2007). Daily variation of surface fine

528   aerosols (dust, sulfate, nitrate, BC, and OC) averaged for 2010-2014 from the IMPROVE

529   measurements and the corresponding model simulations are illustrated in Figure 15. The

530   IMPROVE sites over the western U.S. (Fig. 1) that have measurements for the entire five

531   years (2010-2014) and with less noisy values are divided at 40°N into two groups to

532   represent the Northwest and Southwest U.S. The averaged values over the Northwest and

533   Southwest sites are shown. At the Northwest sites, the model well captures the observed

534   seasonal variation of dust. Both the observations and simulation show the maximum dust

535   mass concentration in MAM. The observed surface sulfate concentrations are the lowest

536   in the cold season when photochemistry is least active, and the highest in the warm

season when the most active photochemistry occurs. This seasonality of sulfate may also be contributed by the seasonality of wet removal (much more precipitation in DJF). Nitrate shows a seasonality that is opposite to that of sulfate, with a maximum surface concentration occurring in the cold season and a minimum in the warm season, which can be explained by the combined effects of temperature and vertical turbulent mixing (Zhao et al., 2013a). The simulation generally reproduces the magnitude and seasonality of both sulfate and nitrate. At the Southwest sites, the simulation is consistent with the observations on the magnitude and seasonality of surface concentrations of dust, surface, and nitrate.

A sensitivity simulation without dust, fire, and anthropogenic emissions over North America (10°N-70°N and 170°W-60°W) indicates that the trans-Pacific transported dust dominates the total dust amount in all seasons at both the northern and southern sites, particularly in MAM. At the southern sites, the North American dust makes a significant contribution in DJF. The sensitivity simulation also shows that trans-Pacific transported sulfate and nitrate can make significant contribution to their surface concentration over the western U.S., and the relative contributions are larger when the surface concentrations are lower (i.e., cold seasons for sulfate and warm seasons for nitrate). During the cold seasons, the North American anthropogenic emissions determine the nitrate surface concentrations. Some differences in dust, sulfate, and nitrate surface concentrations also exist between the observations and simulation. These differences may reflect partly the modeling biases of trans-Pacific aerosols, and also the uncertainties in the North American dust and anthropogenic emissions. Another source of the difference may be from the sub-grid variability of emissions and surface concentrations that

560   confounds the comparison of model simulation at one-degree horizontal grid resolution

561   and the point measurements from the individual sites.

562   There is a significant difference in BC and OC surface concentrations between the

563   observations and simulation. At the Northwest sites, the observed BC and OC show

564   significant seasonal variation with the highest surface concentration in June-September

565   (JJAS). This consistent peak of BC and OC surface concentrations is likely due to the

566   North American biomass burning that also reaches a maximum in JJAS (Chin et al.,

567   2007). The simulation captures this seasonality to some extent but significantly

568   underestimates the JJAS peak for both BC and OC. The sensitivity simulation shows that

569   the peak is dominated by the North American emissions. This significant negative bias in

570   the model is likely from uncertainties in the GFEDv3 biomass burning inventory for the

571   simulation period. The monthly mean emissions at a relatively coarse horizontal

572   resolution may not be able to capture the strong local fire events.

573   At the Southwest sites, the impact of biomass burning on the BC and OC surface

574   concentrations seems relatively small. The simulation can well capture the magnitude and

575   seasonality of surface BC concentration that shows the maximum in DJF and the

576   minimum in JJA, which is likely due to stronger vertical turbulent mixing in JJA

577   compared with DJF. The observed OC still shows peak concentrations in JJA, and the

578   model significantly underestimates the peak OC concentrations. However, this negative

579   bias seems not to be related to the underestimation of biomass burning because BC is

580   reasonably simulated. This seasonal variability may be determined by the secondary

581   production of OC, which peaks in JJA because of more active photochemistry and higher

582   emissions of biogenic VOCs. The underestimation of secondary organic aerosol (SOA)

583   may be due to uncertainty of biogenic emissions (Zhao et al., 2015) and the outdated

584   SOA mechanism used in the current version of WRF-Chem (Shrivastava et al., 2011). On

585   the other hand, it is also noteworthy that uncertainties in the IMPROVE carbonaceous

586   aerosol data are also relatively high because they are inferred from optical/thermal

587   measurements. The sensitivity simulation again shows that the peaks of BC and OC

588   surface concentrations are dominated by the North American emissions.

589

590   **5 Summary and conclusion**

591   A fully coupled meteorology-chemistry model (WRF-Chem) has been configured

592   to conduct quasi-global simulation for the 5 years of 2010-2014. The simulation results

593   are evaluated for first time with various reanalysis and observational datasets, including

594   precipitation from GPCP, wind fields from MERRA, AOD, EAE, and AAOD from

595   MODIS, MISR, OMI, and AERONET, aerosol extinction profiles from CALIPSO, and

596   aerosol surface mass concentrations from IMPROVE. In this study, the evaluation and

597   analysis focus on the trans-Pacific transport region for the purpose of demonstrating the

598   capability of using the quasi-global WRF-Chem simulation to provide consistent lateral

599   chemical boundaries for nested regional WRF-Chem simulations that can be used to

600   investigate the impact of trans-Pacific transported aerosols on the regional air quality and

601   climate over the western US. The main conclusion is summarized below:

602   ▪   The comparison of simulated AOD with the satellite and AERONET retrievals

603   reveals that the model can well capture the spatial gradient of aerosol mass loading

604   decreasing from West to East Pacific, resulting from the sea-salt loading and the

605   Asian pollutant outflow. The seasonal variation of aerosols across Pacific with the

maximum AOD in MAM is also reproduced by the model. The model underestimates AOD over the ocean to the south of 20°N and over the continent of North America against the satellite retrievals. This discrepancy may reflect the model underestimation of marine emissions and/or overestimation of aerosol wet removal or the positive retrieval errors due to cloud-contamination. Compared with the AERONET retrievals, the difference of AOD over the western US between the simulation and satellite retrievals may be due to uncertainty in the satellite retrievals over the continent.

- The assessment of simulated EAE indicates that the model captures the observed smaller-size aerosols over West Pacific contributed by the Asian pollutant outflow compared to the relatively larger particles over Central and East Pacific with more contributions from sea-salt. The model also simulates the consistent seasonality of EAE with observations showing a minimum in DJF and a maximum in JJA due to the active production of small particles in warm seasons.

- The model reasonably simulates the decreasing gradient of OMI derived AAOD from East to West of Pacific, and the seasonality with a peak in MAM due to the strong outflow of dust and anthropogenic pollutants. The comparison with AERONET retrieved AAOD over East Asia may indicate that the OMI SSA retrievals have positive biases over East Asia and also West Pacific that is significantly affected by the East Asian outflow, particularly in JJA. Over East Asia, the model positive biases in AAOD in the warm months may be partly due to the neglect of the seasonal variability of anthropogenic BC emissions in this study.

628   ▪   The model generally captures the CALIPSO retrieved vertical distributions of aerosol

629   extinction coefficients roughly decreasing with the altitude over the Pacific. Near the

630   surface, retrieval uncertainties and model biases in estimating marine aerosol

631   emissions may both contribute to the discrepancy between the simulation and

632   retrievals. The difference between the simulation and retrievals in the free

633   troposphere may be due to the reduced sensitivity of CALIOP to the aerosol layers

634   above 4 km. The model well captures the seasonality of aerosol extinction profiles

635   with a maximum in MAM, which is largely controlled by the activity of dust outflow

636   events over the Pacific.

637   ▪   Compared with the measurements from the IMPROVE sites over the western US, the

638   model reproduces the observed magnitude and seasonality of dust, sulfate, and nitrate

639   surface concentrations, with peaks in MAM, JJA, and DJF, respectively. Over the

640   southwestern U.S., the simulation reproduces the magnitude and seasonality of

641   surface BC concentrations that show the maximum in DJF, but significant

642   underestimates the surface OC concentrations in JJA likely due to the negative biases

643   in SOA production. Over the northwestern U.S., the simulation significantly

644   underestimates surface BC and OC concentrations likely due to the uncertainties in

645   fire emissions of which the monthly variation and the half-degree horizontal

646   resolution may not be sufficient to capture the strong local fire events. Another source

647   of the difference may be due to the discrepancy in spatial scales between site

648   observations and model output for grid cell area of one-degree resolution. In addition,

649   uncertainties in IMPROVE may also contribute to the discrepancy, in particular for

650   carbonaceous aerosols that are inferred from optical/thermal measurements.

651 ▪ The sensitivity simulation shows that the trans-Pacific transported dust dominates the

652 dust surface concentrations in the western US, particularly in MAM. The trans-

653 Pacific transported sulfate and nitrate can also make significant contribution to their

654 surface concentration over the rural areas of the western US, in particular when their

655 surface concentrations are relatively low. The peaks of BC and OC surface

656 concentrations over the western US are dominated by the North American emissions.

657 These sensitivity simulation results may be different to some extent from other

658 models (e.g., Chin et al., 2007), which could result from the considerable differences

659 in aerosol composition and vertical distributions due to differences in model

660 treatments of emissions and removal processes as revealed by several inter-

661 comparison studies (Barrie et al., 2001; Penner et al., 2002; Textor et al., 2006). More

662 detailed model inter-comparison of the trans-Pacific transport of aerosols deserves

663 further study.

664 Although dust and biomass burning emissions in general have considerable year-

665 to-year variations, the interannual variability of seasonal AOD for 2010-2014 averaged

666 over the three sub-regions of Pacific is small as indicated by the retrievals and simulation.

667 It is noteworthy that the trans-Pacific aerosols identified in this study include not only the

668 outflow of Asian pollutants and dust but also European pollutants and African dust that

669 are transported to Asia and then merged with the Asian outflow. This has been

670 recognized by previous studies (e.g., Chin et al., 2007) and also our on-going research

671 (Hu et al., 2015). The evaluation in this study successfully demonstrates that the WRF-

672 Chem quasi-global simulation can be used for studying trans-Pacific transport of aerosols

673 and providing reasonable inflow chemical boundaries for the western U.S. to further

674 understand the impact of transported pollutants on the air quality and regional climate

675 with high resolution nested regional modeling. It needs to be noted that the aerosol

676 optical properties, such as AOD, AAOD, and EAE, derived from the retrievals and

677 simulations have some different assumptions of the physical and optical parameters, so

678 that the link between the model and the satellite data are only qualitative or semi-

679 quantitative. Evaluation of model results with in-situ observations, particularly for a

680 specific event may also be needed, especially over Asia and Pacific, where data are

681 sparse or inaccessible.

682

683 **Code availability**

684 The WRF-Chem version 3.5.1 release can be obtained at

685 http://www2.mmm.ucar.edu/wrf/users/download/get_source.html. A general WRF-Chem

686 user's guide is also available online (http://ruc.noaa.gov/wrf/WG11/). Code modifications

687 and model configuration for conducting quasi-global WRF-Chem simulations here are

688 available upon request by contacting the corresponding author and will be incorporated in

689 the future available release of WRF-Chem.

690

691 **Acknowledgements**

692 This research was supported by the Office of Science of the U.S. Department of Energy

693 (DOE) as part of the Regional & Global Climate Modeling (RGCM) program. J. Huang

694 acknowledges support from the National Basic Research Program of China

695 (2012CB955301). H. Yu was supported by NASA CALIPSO project (NNX14AB21G)

696 managed by Dr. David Considine. This study used computing resources from the PNNL

697   Institutional Computing. Pacific Northwest National Laboratory is operated by Battelle

698   Memorial Institute for the DOE under contract DE-AC05-76RL01830. The CALIPSO

699   data were obtained from the NASA Langley Research Center Atmospheric Sciences Data

700   Center. MODIS and MISR data were obtained from the NASA Atmospheric Science

701   Data Center. OMI data were obtained from the NASA Goddard Earth Sciences Data and

702   Information Services Center.

703

704

Reference

Ahn, C., O. Torres, and P. K. Bhartia: Comparison of Ozone Monitoring Instrument UV Aerosol Products with Aqua/Moderate Resolution Imaging Spectroradiometer and Multiangle Imaging Spectroradiometer observations in 2006, 113, D16S27, doi:10.1029/2007JD008832, 2008.

Anderson, T. L., Y. Wu, D. A. Chu, B. Schmid, J. Redemann, and O. Dubovik: Testing the MODIS satellite retrieval of aerosol fine-mode fraction, J. Geophys. Res., 110, D18204, doi:10.1029/2005JD005978, 2005.

Angstrom, A. : On the atmospheric transmission of Sun radiation and on dust in the air, Geogr. Ann, 11, 156-166, 1929.

Ault, A. P., C. R. Williams, A. B. White, P. J. Neiman, J. M. Creamean, C. J. Gaston, F. M. Ralph, and K. A. Prather: Detection of Asian dust in California orographic precipitation, J. Geophys. Res., 116, D16205, doi:10.1029/2010JD015351, 2011.

Barnard, J. C., J. D. Fast, G. Paredes-Miranda, W. P. Arnott, and A. Laskin: Technical Note: Evaluation of the WRF-Chem "Aerosol Chemical to Aerosol Optical Properties" Module using data from the MILAGRO campaign, Atmos. Chem. Phys., 10, 7325-7340, doi:10.5194/acp-10-7325-2010, 2010.

Barrie, L. A., Y. Yi, W. R. Leaitch, U. Lohmann, P. Kasibhatla, G. J. Roelofs, J. Wilson, F. McGovern, C. Benkovitz, M. A. Melieres, K. Law, J. Prospero, M. Kritz, D. Bergmann, C. Bridgeman, M. Chin, J. Christensen, R. Easter, J. Feichter, C. Land, A. Jeuken, E. Kjellstrom, D. Koch, and P. Rasch: A comparison of large-scale atmospheric sulphate aerosol models (COSAM): overview and highlights, Tellus, 53B, 615-645, 2001.

728   Binkowski, F. S., and Shankar, U.: The Regional Particulate Matter Model 1. Model

729   description and preliminary results, J. Geophys. Res., 100(D12), 26191-26209, 1995.

730   Chapman, E. G., Gustafson Jr., W. I., Easter, R. C., Barnard, J. C., Ghan, S. J., Pekour,

731   M. S., and Fast, J. D.: Coupling aerosol-cloud-radiative processes in the WRF-Chem

732   model: Investigating the radiative impact of elevated point sources, Atmos. Chem.

733   Phys., 9, 945–964, doi:10.5194/acp-9-945-2009, 2009.

734   Chen, S., J. Huang, C. Zhao, Y. Qian, L. R. Leung, and B. Yang: Modeling the transport

735   and radiative forcing of Taklimakan dust over the Tibetan Plateau: A case study in the

736   summer of 2006, J. Geophys. Res., 118(2), 797-812, doi:10.1002/jgrd.50122, 2013.

737   Chen, S., C. Zhao, Y. Qian, L. R. Leung, J. Huang, Z. Huang, J. Bi, W. Zhang, J. Shi, L.

738   Yang, D. Li, J. Li: Regional modeling of dust mass balance and radiative forcing over

739   East   Asia   using   WRF-Chem,   Aeolian   Research,   15,   15-30,

740   doi:10.1016/j.aeolia.2014.02.001, 2014.

741   Chin, M., A. Chu, R. Levy, L. Remer, Y. Kaufman, B. Holben, T. Eck, P. Ginoux, and Q.

742   Gao: Aerosol distribution in the Northern Hemisphere during ACE-Asia: Results

743   from global model, satellite observations, and Sun photometer measurements, J.

744   Geophys. Res., 109, D23S90, doi:10.1029/2004JD004829, 2004.

745   Chin, M., T. Diehl, P. Ginoux, and W. Malm: Intercontinental transport of pollution and

746   dust aerosols: implications for regional air quality, Atmos. Chem. Phys., 7, 5501–

747   5517, 2007.

748   Creamean, J. M., K. J. Suski, D. Rosenfeld, A. Cazorla, P. J. DeMott, R. C. Sullivan, A.

749   B. White, F. M. Ralph, P. Minnis, J. M. Comstock, J. M. Tomlinson, and K. A.

750   Prather: Dust and Biological Aerosols from the Sahara and Asia Influence

751   Precipitation in the Western U.S., Science, 339, 1572, DOI:

752   10.1126/science.1227279, 2013.

753 Dentener, F., S. Kinne, T. Bond, O. Boucher, J. Cofala, S. Generoso, P. Ginoux, S. Gong,

754   J. J. Hoelzemann, A. Ito, L. Marelli, J. E. Penner, J. P. Putaud, C. Textor, M. Schulz,

755   G. R. van der Werf, and J. Wilson: Emissions of primary aerosol and precursor gases

756   in the years 2000 and 1750 prescribed data-sets for AeroCom: Atmos. Chem. Phys.,

757   6, 4321-4344, 2006.

758 Diner, D. J., J. C. Beckert, T. H. Reilly, C. J. Bruegge, J. E. Conel, R. A. Kahn, J. V.

759   Martonchik, T. P. Ackerman, R. Davies, S. A. W. Gerstl, H. R. Gordon, J. P. Muller,

760   R. B. Myneni, P. J. Sellers, B. Pinty, and M. M. Verstraete: Multi-angle Imaging

761   SpectroRadiometer (MISR) Instrument Description and Experiment Overview, IEEE

762   Trans, Geosci. Remote Sens, 36, 1072-1087, 1998.

763 Dubovik, O. and King, M. D.: A flexible inversion algorithm for retrieval of aerosol

764   optical properties from Sum and sky radiance measurements, J. Geophys. Res.,

765   105(16), 20673-20696, 2000.

766 Dubovik, O., B. N. Holben, T. Lapyonok, A. Sinyuk, M. I. Mishchenko, P. Yang, and I.

767   Slutsker: Non-spherical aerosol retrieval method employing light scattering by

768   spheroids, Geophys. Res. Lett., 29(10), 1415, 10.1029/2001GL014506, 2002.

769 Easter, R. C., Ghan, S. J., Zhang, Y., Saylor, R. D., Chapman, E. G., Laulainen, N. S.,

770   Abdul-Razzak, H., Leung, L. R., Bian, X., and Zaveri, R. A.: MIRAGE: Model

771   Description and Evaluation of Aerosols and Trace Gases, J. Geophys. Res., 109,

772   D20210, doi:10.1029/2004JD004571, 2004.

773   Eck, T. F., B. N. Holben, J. S. Reid, O. Dubovik, A. Smirnov, N. T. O'Neill, I. Slutsker,

774   and S. Kinn: Wavelength dependence of the optical depth of biomass burning urban,

775   and desert dust aerosols, , J. Geophys. Res., 104(24), 31333-31349, 1999.

776   Eguchi, K., I. Uno, K. Yumimoto, T. Takemura, A. Shimizu, N. Sugimoto, and Z. Liu:

777   Trans-pacific dust transport: integrated analysis of NASA/CALIPSO and a global

778   aerosol transport model, Atmos. Chem. Phys., 9, 3137–3145, 2009.

779   Fairlie, T. D., D. J. Jacob, and R. J. Park: The impact of transpacific transport of mineral

780   dust in the United States: Atmospheric Environment, 41, 1251-1266, 2007.

781   Fan, J., L. R. Leung, P. J. DeMott, J. M. Comstock, B. Singh, D. Rosenfeld, J. M.

782   Tomlinson, A. White, K. A. Prather, P. Minnis, J. K. Ayers, and Q. Min: Aerosol

783   impacts on California winter clouds and precipitation during CalWater 2011: local

784   pollution versus long-range transported dust, Atmos. Chem. Phys., 14, 81–101,

785   doi:10.5194/acp-14-81-2014, 2014.

786   Fan, J., D. Rosenfeld, Y. Yang, C. Zhao, L. R. Leung, and Z. Li: Substantial contribution

787   of anthropogenic air pollution to catastrophic floods in Southwest China, Geophys.

788   Res. Lett., 42, 6066-6075, doi:10.1002/2015GL064479, 2015.

789   Fast, J. D., W. I. Gustafson, R. C. Easter, R. A. Zaveri, J. C. Barnard, E. G. Chapman, G.

790   A. Grell, and S. E. Peckham: Evolution of ozone, particulates, and aerosol direct

791   radiative forcing in the vicinity of Houston using a fully coupled meteorology-

792   chemistry- aerosol model, J. Geophys. Res., 111, D21305,

793   doi:10.1029/2005JD006721, 2006.

794   Fast, J., A. C. Aiken, J. Allan, L. Alexander, T. Campos, M. R. Canagaratna, E.

795   Chapman, P. F. DeCarlo, B. de Foy, J. Gaffney, J. de Gouw, J. C. Doran, L. Emmons,

796   A. Hodzic, S. C. Herndon, G. Huey, J. T. Jayne, J. L. Jimenez, L. Kleinman, W.

797   Kuster, N. Marley, L. Russell, C. Ochoa, T. B. Onasch, M. Pekour, C. Song, I. M.

798   Ulbrich, C. Warneke, D. Welsh-Bon, C. Wiedinmyer, D. R. Worsnop, X. Y. Yu, and

799   R. Zaveri: Evaluating simulated primary anthropogenic and biomass burning organic

800   aerosols during MILAGRO: implications for assessing treatments of secondary

801   organic aerosols, Atmos. Chem. Phys., 9, 6191–6215, 2009.

802 Fast, J. D., J. Allan, R. Bahreini, J. Craven, L. Emmons, R. Ferrare, P. L. Hayes, A.

803   Hodzic, J. Holloway, C. Hostetler, J. L. Jimenez, H. Jonsson, S. Liu, Y. Liu, A.

804   Metcalf, A. Middlebrook, J. Nowak, M. Pekour, A. Perring, L. Russell, A. Sedlacek,

805   J. Seinfeld, A. Setyan, J. Shilling, M. Shrivastava, S. Springston, C. Song, R.

806   Subramanian, J. W. Taylor, V. Vinoj, Q. Yang, R. A. Zaveri, and Q. Zhang:

807   Modeling regional aerosol and aerosol precursor variability over California and its

808   sensitivity to emissions and long-range transport during the 2010 CalNex and CARES

809   campaigns, Atmos. Chem. Phys., 14, 10013–10060, doi:10.5194/acp-14-10013-2014,

810   2014.

811 Fischer, E. V., N. C. Hsu, D. A. Jaffe, M.-J. Jeong, and S. L. Gong: A decade of dust:

812   Asian dust and springtime aerosol load in the U.S. Pacific Northwest, Geophys. Res.

813   Lett., 36, L03821, doi:10.1029/2008GL036467, 2009.

814 Forster, C., O. Cooper, A. Stohl, S. Eckhardt, P. James, E. Dunlea, D. K. Nicks, J. S.

815   Holloway, G. Hubler, D. D. Parrish, T. B. Ryerson, and M. Trainer: Lagrangian

816   transport model forecasts and a transport climatology for the Intercontinental

817   Transport and Chemical Transformation 2002 (ITCT 2K2) measurement campaign, J.

818   Geophys. Res., 109, D07S92, doi:10.1029/2003JD003589, 2004.

819   Gao, Y., X. Liu, C. Zhao, and M. Zhang: Emission controls versus meteorological

820   conditions in determining aerosol concentrations in Beijing during the 2008 Olympic

821   Games, Atmos. Chem. Phys., 11, 12437–12451, doi:10.5194/acp-11-12437-2011,

822   2011.

823   Gao, Y., C. Zhao, X. H. Liu, M. G. Zhang, and L. R. Leung: WRF-Chem simulations of

824   aerosols and anthropogenic aerosol radiative forcing in East Asia, Atmospheric

825   Environment, 92, 250-266, 2014.

826   Ginoux, P., M. Chin, I. Tegen, J. M. Prospero, B. Holben, O. Dubovik, and S. J. Lin:

827   Sources and distributions of dust aerosols simulated with the GOCART model, J.

828   Geophys. Res., 106(17), 20255-20273, 2001.

829   Gong, S. L.: A parameterization of sea-salt aerosol source function for sub- and super-

830   micron   particles,   Global   Biogeochemical   Cycle,   17(4),   1097,

831   doi:10.1029/2003GB002079, 2003.

832   Grell, G. A., S. E. Peckham, R. Schmitz, S. A. McKeen, G. Frost, W. C. Skamarock, and

833   B. Eder: Fully coupled ''online'' chemistry within the WRF model, Atmospheric

834   Enviroment, 39, 6957-6957, doi:10.1016/j.atmosenv.2005.04.027, 2005.

835   Gustafson, W. I., E. G. Chapman, S. J. Ghan, R. C. Easter, and J. D. Fast: Impact on

836   modeled cloud characteristics due to simplified treatment of uniform cloud

837   condensation nuclei during NEAQS 2004, Geophys. Res. Lett., 34, L19809,

838   doi:10.1029/2007GL030021, 2007.

839   Hadley, O. L., V. Ramanathan, G. R. Carmichael, Y. Tang, C. E. Corrigan, G. C.

840   Roberts, and G. S. Mauger: Trans-Pacific transport of black carbon and fine aerosols

841   (D < 2.5 mm) into North America, J. Geophys. Res., 112, D05309,

842   doi:10.1029/2006JD007632, 2007.

843   Hadley, O. L., C. E. Corrigan, T. W. Kirchstetter, S. S. Cliff, and V. Ramanathan:

844   Measured black carbon deposition on the Sierra Nevada snow pack and implication

845   for snow pack retreat, Atmos. Chem. Phys., 10, 7505-7513, doi:10.5194/acp-10-

846   7505-2010, 2010.

847   Hand, J., S. A. Copeland, D. E. Day, A. M. Dillner, H. Indresand, W. C. Malm, C. E.

848   McDade, C. T. Moore, Jr, M. L. Pitchford, B. A. Schichtel, and J. G. Watson: Spatial

849   and seasonal patterns and temporal variability of haze and its constituents in the

850   United   States: Report   V,   June,   2011,   available   from

851   http://vista.cira.colostate.edu/improve/Publications/ Reports/2011/2011.htm, 2011.

852   Heald, C. L., D. J. Jacob, R. J. Park, B. Alexander, T. D. Fairlie, R. M. Yantosca, and D.

853   A. Chu: Transpacific transport of Asian anthropogenic aerosols and its impact on

854   surface air quality in the United States, J. Geophys. Res., 111, D14310,

855   doi:10.1029/2005JD006847, 2006.

856   Hess, M., P. Koepke, and I. Schult: Optical Properties of Aerosols and Clouds: The

857   Software Package OPAC, Bull. Am. Meteorol. Soc., 79(5), 831-844, 1998.

858   Holben, B. N., T. F. Eck, I. Slutsker, D. Tanré, J. P. Buis, A. Setzer, E. Vermote, J. A.

859   Reagan, Y. J. Kaufman, T. Nakajima, F. Lavenu, I. Jankowiak, and A. Smirnov:

860   AERONET - A Federated Instrument Network and Data Archive for Aerosol

861   Characterization, Remote Sens. Environ., 66, 1-16, 1998.

862   Holben, B. N., D. Tanr, A. Smirnov, T. F. Eck, I. Slutsker, N. Abuhassan, W. W.

863   Newcomb, J. S. Schafer, B. Chatenet, F. Lavenu, Y. J.Kaufman, J. V. Castle, A.

864   Setzer, B. Markham, D. Clark, R. Frouin, R. Halthore, A. Karneli, N. T. O'Neill, C.

865   Pietras, R. T. Pinker, K. Voss, and G. Zibordi: An emergingground-

866   basedaerosolclimatology: Aerosol optical depth from AERONET, J. Geophys. Res.,

867   106(11), 12067-12097, 2001.

868   Hsu, N. C., S. C. Tsay, M. D. King, and J. R. Herman: Deep Blue Retrievals of Asian

869   Aerosol Properties During ACE-Asia, IEEE Trans, Geosci. Remote Sens., 44(11),

870   3180-3195, 2006.

871   Hsu, N. C., M.-J. Jeong, and C. Bettenhausen: Enhanced Deep Blue aerosol retrieval

872   algorithm: The second generation, J. Geophys. Res. Atmos., 118 (16): 9296–9315,

873   2013.

874   Hu, Z., C. Zhao, J. Huang, L. R. Leung, and Y. Qian: Transpacific transport and

875   evolution of aerosols: Source contribution analysis, manuscript in preparation.

876   Huang, L., J. H. Jiang, J. L. Tackett, H. Su, and R. Fu: Seasonal and diurnal variations of

877   aerosol extinction profile and type distribution from CALIPSO 5-year observations, J.

878   Geophys. Res. Atmos., 118, 4572–4596, doi:10.1002/jgrd.50407, 2013.

879   Huffman, G. J., R. F. Adler, M. M. Morrissey, D. T. Bolvin, S. Curtis, R. Joyce, B.

880   McGavock, and J. Susskind: Global Precipitation at One-Degree Daily Resolution

881   from   Multisatellite   Observations.   J.   Hydrometeor,   2,   36–50,doi:

882   http://dx.doi.org/10.1175/1525-7541(2001)002<0036:GPAODD>2.0.CO;2, 2001.

883   Iacono, M. J., E. J. Mlawer, S. A. Clough, and J. J. Morcrette: Impact of an

884   improvedlongwaveradiation model,RRTM, on the energy budget and thermodynamic

885   properties of the NCAR community climate model, CCM3, J. Geophys. Res.,

886   105(11), 14873-14890, 2000.

887   Jaegle, L., P. K. Quinn, T. S. Bates, B. Alexander, and J. T. Lin: Global distribution of

888   sea salt aerosols: new constraints from in situ and remote sensing observations,

889   Atmos. Chem. Phys., 11, 3137-3157, doi:10.5194/acp-11-3137-2011, 2011.

890   Jaffe, D., T. Anderson, D. Covert, R. Kotchenruther, B. Trost, J. Danielson, W. Simpson,

891   T. Berntsen, S. Karlsdottir, D. Blake, J. Harris, G. Carmichael, and I. Uno: Transport

892   of Asian Air Pollution to North America, Geophys. Res. Lett., 26(6), 711-714, 1999.

893   Jethva, H., O, Torres, and C. Ahn: Global assessment of OMI aerosol single-scattering

894   albedo using ground-based AERONET inversion, J. Geophys. Res. Atmos., 119,

895   9020–9040, doi:10.1002/ 2014JD021672, 2014.

896   Kahn, R. A., D. L. Nelson, M. J. Garay, R. C. Levy, M. A. Bull, D. J. Diner, J. V.

897   Martonchik, S. R. Paradise, E. G. Hansen, and L. A. Remer: MISR Aerosol Product

898   Attributes and Statistical Comparisons With MODIS, IEEE Trans, Geosci. Remote

899   Sens, 47(12), 4095-4114, 2009.

900   Kaufman, Y. J., D. Tanré, L. A. Remer, E. F. Vermote, A. Chu, and B. N. Holben:

901   Operational remote sensing of tropospheric aerosol over land from EOS moderate

902   resolution imaging spectroradiometer, J. Geophys. Res., 102(D14), 17051-17067,

903   1997.

904   Kaufman, Y. J., O. Boucher,D. Tanre, M. Chin, L. A. Remer, and T. Takemura: Aerosol

905   anthropogenic component estimated from satellite data, Geophys. Res. Lett., 32,

906   L17804, doi:10.1029/2005GL023125, 2005a.

907   Kaufman, Y. J., I. Koren, L. A. Remer, D. Rosenfeld, and Y. Rudich: The effect of

908   smoke, dust, and pollution aerosol on shallow cloud development over the Atlantic

909   Ocean, Proc. Natl. Acad. Sci. USA, 102(32), 11207-11212,

910   Doi/10.1073/pnas.0505191102, 2005b.

911   King, M. D., Y. J. Kaufman, D. Tanre, and T. Nakajima: Remote Sensing of

912   Tropospheric Aerosols from Space: Past, Present, and Future, Bull. Am. Meteorol.

913   Soc., 80(11), 2229-2259, 1999.

914   Kok, J. F.: A scaling theory for the size distribution of emitted dust aerosols suggests

915   climate models underestimate the size of the global dust cycle, Proc. Natl. Acad. Sci.

916   USA, 108(3), 1016-1021, doi/10.1073/pnas.1014798108, 2011.

917   Koren, I., Y. J. Kaufman, D. Rosenfeld, L. A. Remer, and Y. Rudich: Aerosol

918   invigoration and restructuring of Atlantic convective clouds, Geophys. Res. Lett., 2,

919   L14828, doi:10.1029/2005GL023187, 2005

920   Levy, R. C., L. A. Remer, R. G. Keidman, S. Mattoo, C. Ichoku, R. Kahn, and T. F. Eck:

921   Global evaluation of the Collection 5 MODIS dark-target aerosol products over land,

922   Atmos. Chem. Phys., 10, 10399–10420, doi:10.5194/acp-10-10399-2010, 2010.

923   Levy, R. C., S. Mattoo, L. A. Munchak, L. A. Remer, A. M. Sayer, F. Patadia, and N.

924   Hsu: The Collection 6 MODIS Aerosol Products over Land and Ocean, Atmos. Meas.

925   Tech., 6, 2989-3034 doi:10.5194/amt-6-2989-2013, 2013.

926   Liang, Q., L. Jaegle, D. A. Jaffe, P. Weiss-Penzias, A. Heckman, and J. A. Snow: Long-

927   range transport of Asian pollution to the northeast Pacific: Seasonal variations and

928   transport pathways of carbon monoxide, J. Geophys. Res., 109, D23S07,

929   doi:10.1029/2003JD004402, 2004.

930   Liu, Z., M. A. Vaughan, D. M. Winker, C. A. Hostetler, L. R. Poole, D. Hlavka, W. Hart,

931   abd M. McGill: Use of probability distribution functions for discriminating between

932   cloud and aerosol in lidar backscatter data, J. Geophys. Res., 109, D15202,

933   doi:10.1029/2004JD004732, 2004.

934   Lu, Z., D. G. Streets, Q. Zhang, S. Wang, G. R. Carmichael, Y. F. Cheng, C. Wei, M.

935   Chin, T. Diehl, and Q. Tan: Sulfur dioxide emissions in China and sulfur trends in

936   East Asia since 2000, Atmos. Chem. Phys., 10, 6311-6331, doi:10.5194/acp-10-6311-

937   2010, 2010.

938   Lu, Z., Q. Zhang, and D. G. Streets: Sulfur dioxide and primary carbonaceous aerosol

939   emissions in China and India, 1996–2010, Atmos. Chem. Phys., 11, 9839-9864,

940   doi:10.5194/acp-11-9839-2011, 2011.

941   Malm, W. C., J. F. Sisler, D. Huffman, R. A. Eldred, and T. A. Cahill: Spatial and

942   seasonal trends in particle concentration and optical extinction in the United States,

943   99(D1), 1347-1370, 1994.

944   Martonchik, J. V., David J. D., Kathleen A. C., and M. A. Bull: Regional Aerosol

945   Retrieval Results From MISR, IEEE Trans, Geosci. Remote Sens, 40(7), 1520-1531,

946   2002.

947   McKeen, S. A., G. Wotawa, D. D. Parrish, J. S. Holloway, M. P. Buhr, G. Hubler, F. C.

948   Fehsenfeld, and J. F. Meagher: Ozone production from Canadian wildfires during

949   June and July of 1995, J. Geophys. Res., 107(D14), 4192, 10.1029/2001JD000697,

950   2002.

951   Mlawer, E. J., S. J. Taubman, P. D. Brown, M. J. Iacono, and S. A. Clough: Radiative

952   transfer for inhomogeneous atmospheres: RRTM, a validated correlated-k model for

953   the longwave, J. Geophys. Res., 102(D14), 16663-16682, 1997.

954   Painter, T. H., J. S. Deems, J. Belnap, A. F. Hamlet, C. C. Landry, and B. Udall:

955   Response of Colorado River runoff to dust radiative forcing in snow, Proc. Natl.

956   Acad. Sci. USA, 107(40), 17125-17130, doi/10.1073/pnas.0913139107, 2010.

957   Penner, J. E., S. Y. Zhang, M. Chin, C. C. Chuang, J. Fechter, Y. Feng, I. V.

958   Geogdzhayev, P. Ginoux, M. Herzog, A. Higurashi, D. Koch, C. Land, U. Lohmann,

959   M. Mischecko, T. Nakajima, G. Pitari, B. Soden, I. Tegen, and L. Stowe: A

960   Comparison of Model- and Satellite-Derived Aerosol Optical Depth and Reflectivity,

961   J. Atmos. Sci., 59, 441-460, 2002.

962   Qian, Y., W. I. Gustafson, L. R. Leung, and S. J. Ghan: Effects of soot-induced snow

963   albedo change on snowpack and hydrological cycle in western United States based on

964   Weather Research and Forecasting chemistry and regional climate simulations, J.

965   Geophys. Res., 114, D03108, doi:10.1029/2008JD011039, 2009.

966   Qian, Y., W. I. Gustafson Jr. and J. D. Fast: An investigation of the sub-grid variability of

967   trace gases and aerosols for global climate modeling, Atmos. Chem. Phys., 10, 6917-

968   6946, doi:10.5194/acp-10-6917-2010, 2010.

969   Qian, Y., H. Yan, Z. Hou, C. Johannesson, S. Klein, D. Lucas, R. Neale, P. Rasch, L.

970   Swiler, J. Tannahill, H. Wang, M. Wang, and C. Zhao: Parametric sensitivity analysis

971   of precipitation at global and local scales in the Community Atmosphere Model

972   CAM5, J. Adv. Model. Earth Syst., 7, 382-411, doi:10.1002/2014MS000354, 2015.

973   Remer, L. A., Y. J. Kaufman, D. Tanre, S. Mattoo, D. A. Chu, J. V. Martins, R. R. Li, C.

974   Ichoku, R. C. Levy, R. G. Kleidman, T. F. Eck, E. Vermote, and B. N. Holben: The

975   MODIS aerosol algorithm, products and validation, J. Atmos. Sci., 62, 947-973,

976   2005.

977   Remer, L. A. and Kaufman, Y. J.: Aerosol direct radiative effect at the top of the

978   atmosphere over cloud free ocean derived from four years of MODIS data, Atmos.

979   Chem. Phys., 6, 237–253, 2006.

980   Rienecker, M. M., M. J. Suarez, R. Gelaro, R. Todling, J. Bacmeister, E. Liu, M. G.

981   Bosilovich, S. D. Schubert, L. Takacs, G.-K. Kim, S. Bloom, J. Chen, D. Collins, A.

982   Conaty, A. da Silva, W. Gu, J. Joiner, R. D. Koster, R. Lucchesi, A. Molod, T.

983   Owens, S. Pawson, P. Pegion, C. R. Redder, R. Reichle, F. R. Robertson, A. G.

984   Ruddick, M. Sienkiewicz, and J. Woollen: MERRA: NASA's Modern-Era

985   Retrospective Analysis for Research and Applications. J. Climate, 24, 3624–3648.

986   doi: http://dx.doi.org/10.1175/JCLI-D-11-00015.1, 2011.

987   Sassen, K.: Indirect climate forcing over the western US from Asian Dust strom,

988   Geophys. Res. Lett., 29(10), 1465, 10.1029/2011GL014051, 2002.

989   Schulz, M., C. Textor, S. Kinne, Y. Balkanski, S. Bauer, T. Berntsen, T. Berglen, O.

990   Boucher, F. Dentener, S. Guibert, I. S. A. Isaksen, T. Iversen, D. Koch, A. Kirkevag,

991   X. Liu, V. Montanaro, G. Myhre, J. E. Penner, G. Pitari, S. Reddy, Ø. Seland, P.

992   Stier, and T. Takemura: Radiative forcing by aerosols as derived from the AeroCom

993   present-day and pre-industrial simulations, Atmos. Chem. Phys., 6, 5225–5246, 2006.

994   Schuster, G. L., O. Dubovik, and B. N. Holben: Angstrom exponent and bimodal aerosol

995   size distributions, J. Geophys. Res., 111, D07207, doi:10.1029/2005JD006328, 2006.

996   Shrivastava, M., J. Fast, R. Easter, W. I. Gustafson, R. A. Zaveri, J. L. Jimenez, P. Saide,

997   and A. Hodzic: Modeling organic aerosols in a megacity: comparison of simple and

998   complex representations of the volatility basis set approach, 11, 6639–6662,

999   doi:10.5194/acp-11-6639-2011, 2011.

1000 Skamarock, W. C. and Klemp, J. B.: A time-split nonhydrostatic atmospheric model for

1001 weather research and forecasting applications, J. Com. Phy., 227, 3456-3485,

1002 doi:10.1016/j.jcp.2007.01.037, 2008.

1003 Stauffer, D. R. and Seaman, N. L.: Use of Four-Dimensional Data Assimilation in a

1004 Limited_Area Mesoscale Model. Part I: Experiments with Synoptic-Scale Data, Mon.

1005 Wea. Rev., 118, 1250-1277, 1990.

1006 Tao, Z., H. Yu, and M. Chin, Impact of transpacific aerosol on air quality over the United

1007 States: A perspective from aerosol-cloud-radiation interactions, Atmos. Environ.,

1008 125, 48-60, 2016.

1009 Textor, C., M. Schulz, S. Guibert, S. Kinne, Y. Balkanski, S. Bauer, T. Berntsen, T.

1010 Berglen, O. Boucher, M. Chin, F. Dentener, T. Diehl, R. Easter, H. Feichter, D.

1011 Fillmore, S. Ghan, P. Ginoux, S. Gong, A. Grini, J. Hendricks, L. Horowitz, P.

1012 Huang, I. Isaksen, T. Iversen, S. Kloster, D. Koch, A. Kirkevag, J. E. Kristjansson,

1013 M. Krol, A. Lauer, J. F. Lamarque, X. Liu, V. Montanaro, G. Myhre, J. Penner, G.

1014 Pitari, S. Reddy, Ø. Seland, P. Stier, T. Takemura, and X. Tie: Analysis and

1015 quantification of the diversities of aerosol life cycles within AeroCom, Atmos. Chem.

1016 Phys., 6, 1777–1813, 2006.

1017 Torres, O., C. Ahn, and Z. Chen: Improvements to the OMI near-UV aerosol algorithm

1018 using A-train CALIOP and AIRS observations, Atmos. Meas. Tech., 6, 3257–3270,

1019 doi:10.5194/amt-6-3257-2013, 2013.

1020 VanCuren, R. A.: Asian aerosols in North America: Extracting the chemical composition

1021 and mass concentration of the Asian continental aerosol plume from long-term

1022   aerosol records in the western United States, J. Geophys. Res., 108, NO. D20, 4623,

1023   doi:10.1029/2003JD003459, 2003.

1024   van der Werf, G. R., J. T. Randerson, L. Giglio, G. J. Collatz, M. Mu, P. S. Kasibhatla, D.

1025   C. Morton, R. S. DeFries, Y. Jin, and T. T. van Leeuwen: Global fire emissions and

1026   the contribution of deforestation, savanna, forest, agricultural, and peat fires (1997–

1027   2009), Atmos. Chem. Phys., 10, 11707–11735, doi:10.5194/acp-10-11707-2010,

1028   2010.

1029   Veihelmann, B., P. F. Levelt, P. Stammes, and J. P. Veefkind: Simulation study of the

1030   aerosol information content in OMI spectral reflectance measurements, Atmos.

1031   Chem. Phys., 7, 3115–3127, 2007.

1032   Winker, D. M., W. H. Hunt, and M. J. McGill: Initial performance assessment of

1033   CALIOP, J. Geophys. Res., 34, L19803, doi:10.1029/2007GL030135, 2007.

1034   Winker, D. M., M. A. Vaughan, A. Omar, Y. Hu, K. A. Powell, Z. Liu, W. H. Hunt, and

1035   S. A. Young: Overview of the CALIPSO Mission and CALIOP Data Processing

1036   Algorithms,   J.   Atmos.   Oceanic   Technol.,   26,   2310–2323,   doi:

1037   http://dx.doi.org/10.1175/2009JTECHA1281.1, 2009.

1038   Yu, H. B., R. E. Dickinson, M. Chin, Y. J. Kaufman, B. N. Holben, I. V. Geogdzhayev,

1039   and M. I. Mishchenko: Annual cycle of global distributions of aerosol optical depth

1040   from integration of MODIS retrievals and GOCART model simulations, J. Geophys.

1041   Res.,108, NO. D3, 4128, doi:10.1029/2002JD002717, 2003.

1042   Yu, H. B., R. E. Dickinson, M. Chin, Y. J. Kaufman, M. Zhou, L. Zhou, Y. Tian, O.

1043   Dubovik, and B. N. Holben: Direct radiative effect of aerosols as determined from a

1044   combination of MODIS retrievals and GOCART simulations, J. Geophys. Res.,109,

1045   D03206, doi:10.1029/2003JD003914, 2004.

1046   Yu, H. B., R. Fu, R. E. Dickinson, Y. Zhang, M. Chen, and H. Wang, Interannual

1047   variability of smoke and warm cloud relationships in the Amazon as inferred from

1048   MODIS   retrievals,   Remote   Sens.   Environ.,   111,   435-449,

1049   doi:10.1016/j.rse.2007.04.003, 2007.

1050   Yu, H. B., L. A. Remer, M. Chin, H. S. Bian, R. G. Kleidman, and T. Diehl: A satellite-

1051   based assessment of transpacific transport of pollution aerosol, J. Geophys. Res., 113,

1052   D14S12, doi:10.1029/2007JD009349, 2008.

1053   Yu, H., M. Chin, L. A. Remer, R. G. Kleidman, N. Bellouin, H. Bian, and T. Diehl:

1054   Variability of marine aerosol fine-mode fraction and estimates of anthropogenic

1055   aerosol component over cloud-free oceans from MODIS, J. Geophys. Res., 114,

1056   D10206, doi:10.1029/2008JD010648, 2009.

1057   Yu, H. B., M. Chin, D. M. Winker, A. H. Omar, Z. Y. Liu, C. Kittaka, and T. Diehl:

1058   Global view of aerosol vertical distributions from CALIPSO lidar measurements and

1059   GOCART simulations: Regional and seasonal variations, J. Geophys. Res.,115,

1060   D00H30, doi:10.1029/2009JD013364, 2010.

1061   Yu, H., L. A. Remer, M. Chin, H. Bian, Q. Tan, T. Yuan, and Y. Zhang: Aerosols from

1062   Overseas Rival Domestic Emissions over North America, Science, 337, 566-569,

1063   2012.

1064   Yu, H., M. Chin, H. Bian, T. L. Yuan, J. M. Prospero, A. H. Omar, L. A. Remer, D. M.

1065   Winker, Y. Yang, Y. Zhang, and Z. Zhang: Quantification of trans-Atlantic dust

1066   transport from seven-year (2007-2013) record of CALIPSO lidar measurements,

1067   Remote Sens. Environ., 159, 232-249, http://dx.doi.org/10.1016/j.rse.2014.12.010,

1068   2015.

1069   Zaveri, R. A. and Peters, L. K.: A new lumped structure photochemical mechanism for

1070   large-scale applications, J. Geophys. Res., 104(D23), 30387-30415, 1999.

1071   Zaveri, R. A., R. C. Easter, J. D. Fast, and L. K. Peters: Model for Simulating Aerosol

1072   Interactions and Chemistry (MOSAIC), J. Geophys. Res., 113, D13204,

1073   doi:10.1029/2007JD008782, 2008.

1074   Zhang, J. and Reid, J. S.: MODIS aerosol product analysis for data assimilation:

1075   Assessment of over-ocean level 2 aerosol optical thickness retrievals, J. Geophys.

1076   Res., 111, D22207, doi:10.1029/2005JD006898, 2006.

1077   Zhang, Q., D. G. Streets, G. R. Carmichael, K. B. He, H. Huo, A. Kannari, Z. Klimont, I.

1078   S. Park, S. Reddy, J. S. Fu, D. Chen, L. Duan, Y. Lei, L. T. Wang, and Z. L. Yao:

1079   Asian emissions in 2006 for the NASA INTEX-B mission, Atmos. Chem. Phys., 9,

1080   5131–5153, 2009.

1081   Zhao, C., X. Liu, L. R. Leung, B. Johnson, S. A. McFarlane, W. I. Gustafson, J. D. Fast,

1082   and R. Easter: The spatial distribution of mineral dust and its shortwave radiative

1083   forcing over North Africa: modeling sensitivities to dust emissions and aerosol size

1084   treatments, Atmos. Chem. Phys., 10, 8821–8838, doi:10.5194/acp-10-8821-2010,

1085   2010a.

1086   Zhao, C., Y. Wang, Q. Yang, R. Fu, and Y. Choi: Impact of East Asia summer monsoon

1087   on the air quality over China: view from space, J. Geophys. Res., 115, D09301,

1088   doi:10.1029/2009JD012745, 2010.

1089   Zhao, C., X. Liu, L. R. Leung, and S. Hagos: Radiative impact of mineral dust on

1090   monsoon precipitation variability over West Africa, Atmos. Chem. Phys., 11, 1879-

1091   1893, doi:10.5194/acp-11-1879-2011, 2011.

1092   Zhao, C., X. Liu, and L. R. Leung: Impact of the Desert dust on the summer monsoon

1093   system over Southwestern North America, Atmos. Chem. Phys., 12, 3717–3731, d

1094   oi:10.5194/acp-12-3717-2012, 2012.

1095   Zhao, C., L. R. Leung, R. Easter, J. Hand, and J. Avise: Characterization of speciated

1096   aerosol direct radiative forcing over California, J. Geophys. Res., 118, 2372–2388,

1097   doi:10.1029/2012JD018364, 2013a.

1098   Zhao, C., S. Chen, L. R. Leung, Y. Qian, J. F. Kok, R. A. Zaveri, and J. Huang:

1099   Uncertainty in modeling dust mass balance and radiative forcing from size

1100   parameterization, Atmos. Chem. Phys., 13, 10733–10753, doi:10.5194/acp-13-10733-

1101   2013, 2013b.

1102   Zhao, C., Z. Hu, Y. Qian, L. R. Leung, J. Huang, M. Huang, J. Jin, M. G. Flanner, R.

1103   Zhang, H. Wang, H. Yan, Z. Lu, and D. G. Streets: Simulating black carbon and dust

1104   and their radiative forcing in seasonal snow: a case study over North China with field

1105   campaign measurements, Atmos. Chem. Phys., 14, 11475–11491, doi:10.5194/acp-

1106   14-11475-2014, 2014.

1107   Zhao, C., M. Huang, J. Fast, L. Berg, Y. Qian, A. Guenther, D. Gu, M. Shrivastava, Y.

1108   Liu, S. Walters, G. Pfister, J. Jin: Sensitivity of biogenic volatile organic compounds

1109   (BVOCs) to land surface processes and vegetation distributions in California,

1110   submitted to *Geosci. Model Dev.*

1111

1112

1113

1114

1115

1116
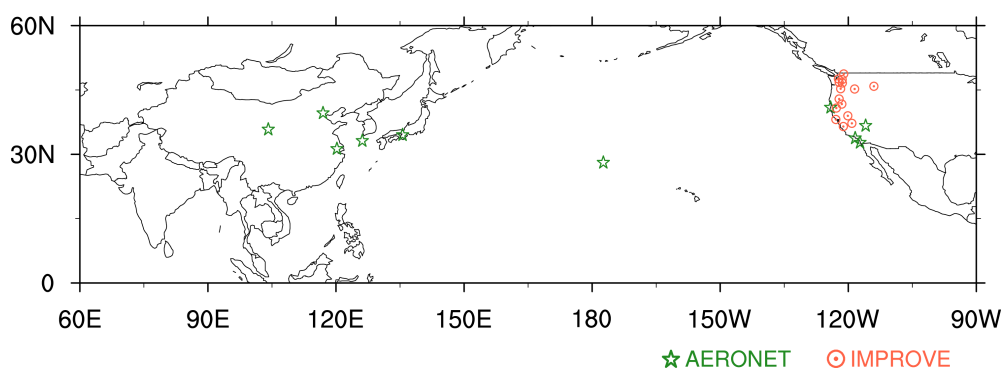
1117

Figure 1 Observation sites for the AERONET (green stars) and IMPROVE (red dot

circle) networks used in this study.

1120

1121

1122

1123

1124

1125

1126

1127

1128

1129

1130

1131

1132

1133

1134

Figure 2 Spatial distributions of seasonal averaged wind fields at 850hPa from MERRA

reanalysis and WRF-Chem simulations for the period of 2010-2014.
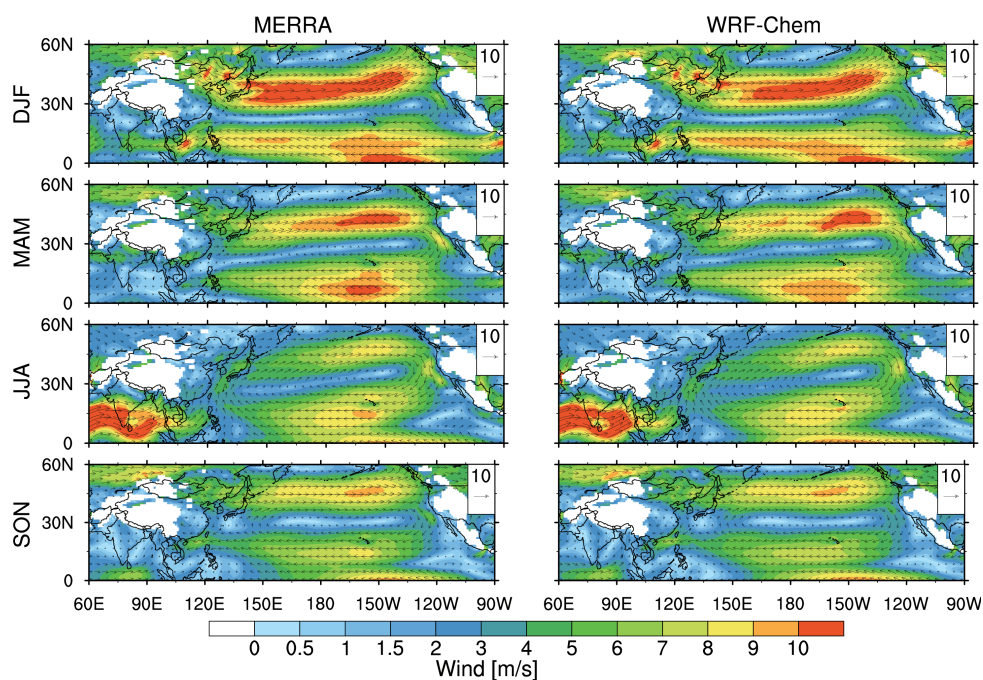
1137

1138

1139

1140

1141

1142

1143

1144

1145

1146

Figure 3 Spatial distributions of seasonal averaged precipitation from GPCP observations

and WRF-Chem simulations for the period of 2010-2014.

1149

1150

1151

1152

1153

1154

1155

1156

1157

1158

1159
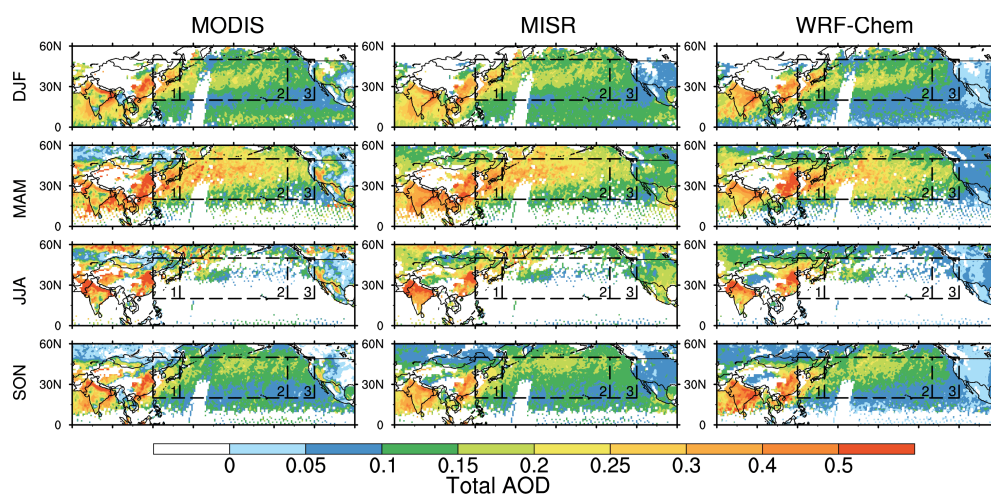
1160

Figure 4 Spatial distributions of seasonal mean 550 nm AOD from the retrievals of

MODIS and MISR onboard Terra and the WRF-Chem simulations for the period of

2010-2014. The daily results from MISR, MODIS, and WRF-Chem are only sampled for

average when all of them have valid values at the same location and time. Three sub-

regions are denoted by the black boxes: Region 1 (20° N-50° N and 120° E-140° E),

Region 2 (20° N-50° N and 140° E-140° W), and Region 3 (20° N-50° N and 140° W-120°

W).

1168

1169

1170

1171

1172

1173

1174

1175
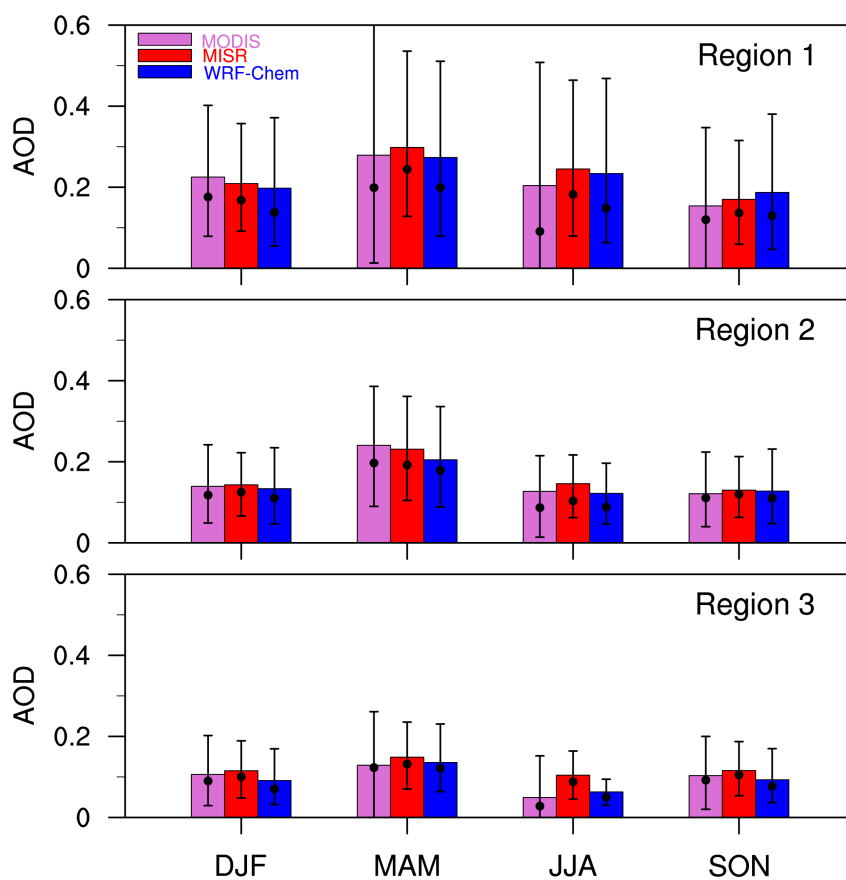
1176

1177 **Figure 5** Seasonal mean 550nm AOD from MISR and MODIS retrievals, and the

1178 corresponding WRF-Chem simulations averaged for 2010-2014, over the three sub-

1179 regions shown in Fig. 4. The values of bars represent the mean. The vertical lines

1180 represent 10th and 90th percentile values, and the black dots represent the median values.

1181

1182

1183
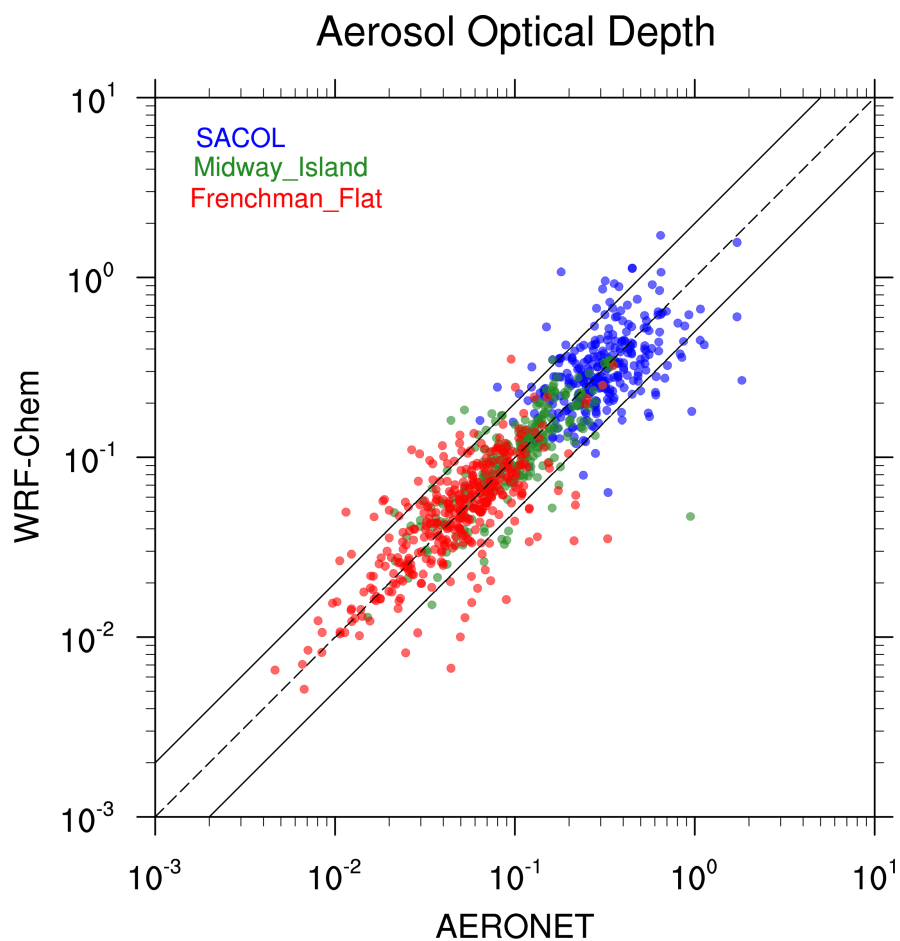
1184

Figure 6 The AERONET observations of daily AOD at 550 nm at the three sites

(SACOL, Midway Island, and Frenchman Flat) versus the corresponding WRF-Chem

simulations for 2010-2014.

1188

1189

1190

1191

1192
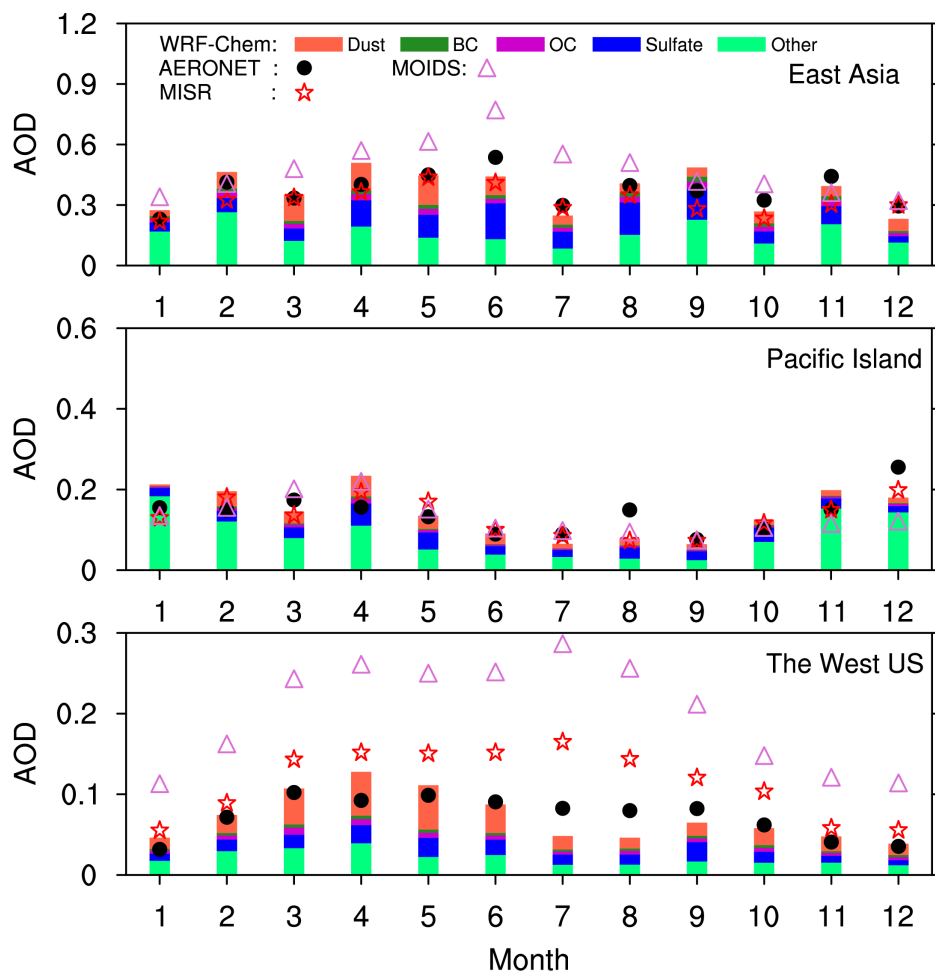
Figure 7 Monthly mean 550nm AOD from AERONET (black dots), MODIS (purple

triangles), MISR (red five-pointed stars) and the corresponding WRF-Chem simulations

(histogram) averaged for 2010-2014 at the East Asian sites, the Pacific island, and the

West U.S. sites as shown in Fig. 1.

1198

1199

1200
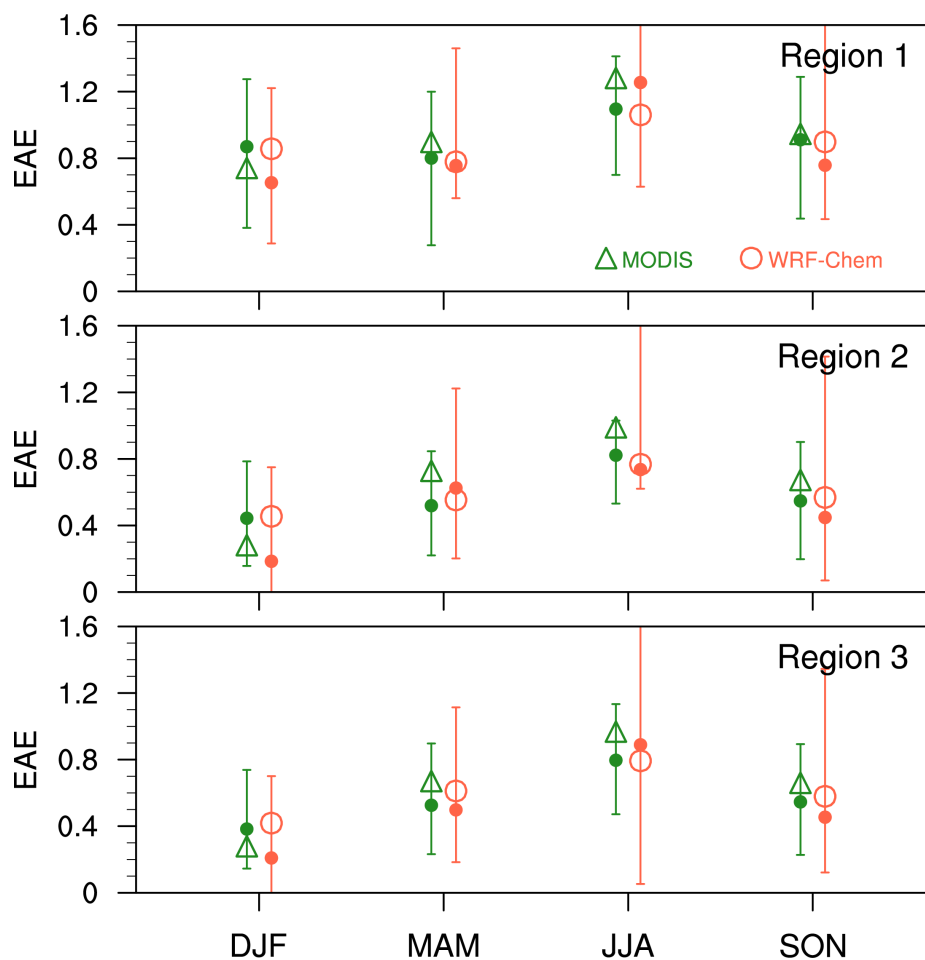
1201

1202 **Figure 8** Seasonal mean EAE from the MODIS retrievals and the corresponding WRF-

1203 Chem simulations averaged for 2010-2014, over the three sub-regions shown in Fig. 4.

1204 The vertical bars represent 10th and 90th percentile values, and the black dots represent the

1205 median values.

1206

1207

1208

1209

1210
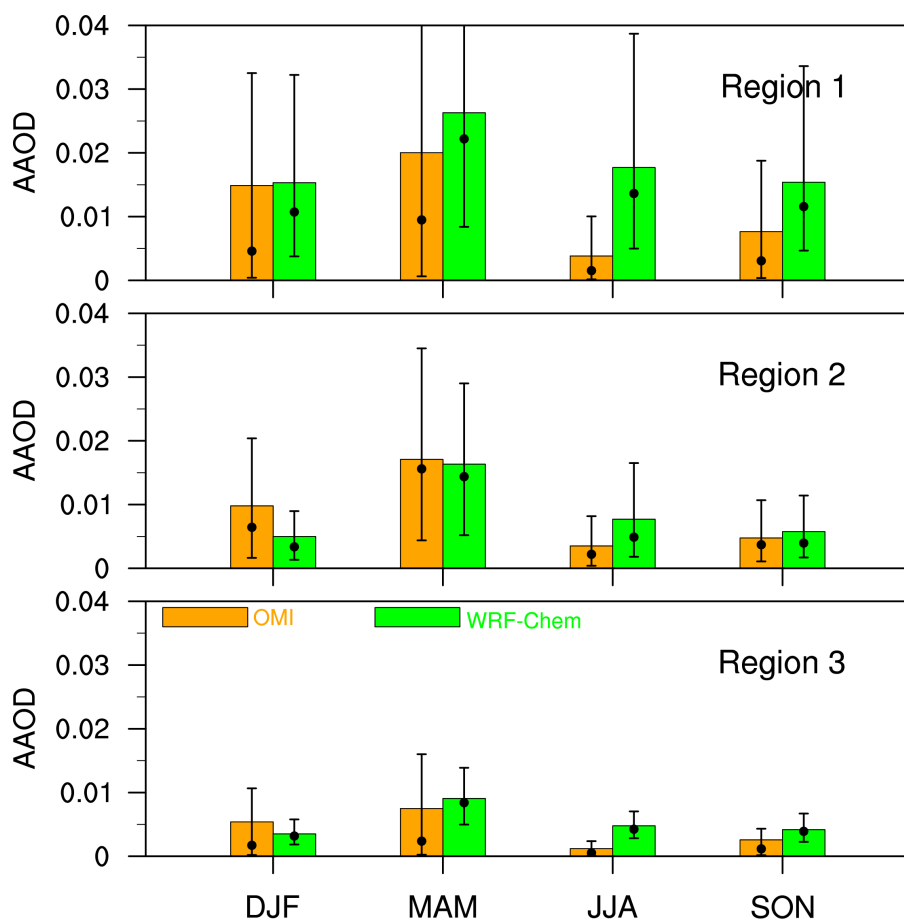
1211

1212 **Figure 9** Seasonal mean AAOD at 500 nm from the OMI retrievals and the

1213 corresponding WRF-Chem simulations averaged for 2010-2014, over the three sub-

1214 regions shown in Fig. 4. The values of bars represent the mean. The vertical lines

1215 represent 10th and 90th percentile values, and the black dots represent the median values.

1216

1217

1218

1219

1220

1221

1222

1223
1224 **Figure 10** Monthly AAOD from the retrievals of AERONET and OMI and the

1225 corresponding WRF-Chem simulations averaged for 2010-2014 over the East Asia sites
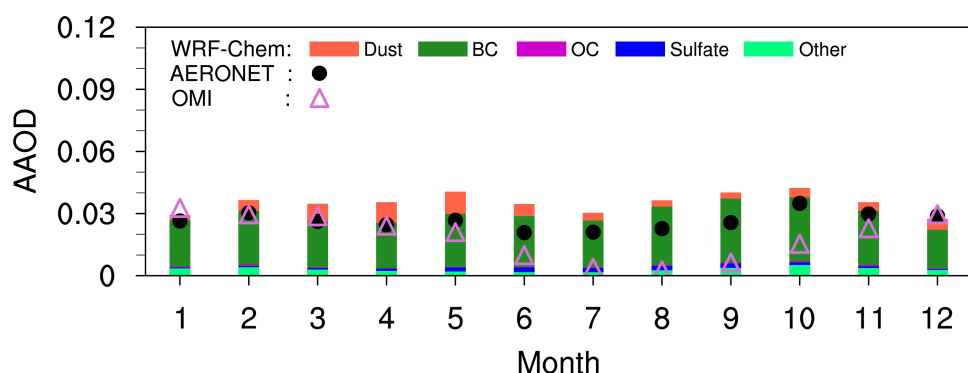
1226 as shown in Fig. 1.

1227

1228

1229

1230

1231

1232

1233

1234

1235

1236

1237
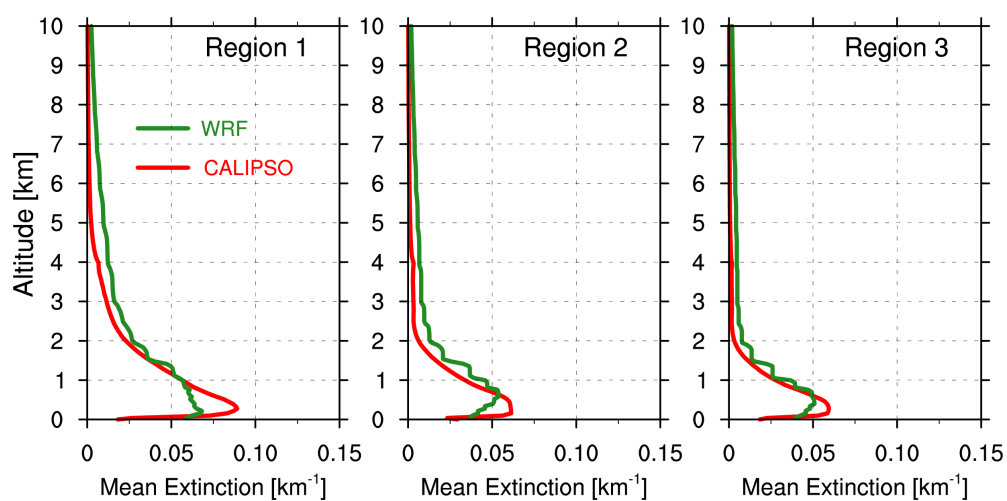
1238

1239   **Figure 11** Annual vertical distributions of extinction from CALIPSO observations and

1240   the corresponding WRF-Chem simulations averaged for 2010-2014, over the three sub-

1241   regions shown in Fig. 4.

1242

1243

1244

1245

1246

1247

1248

1249

1250
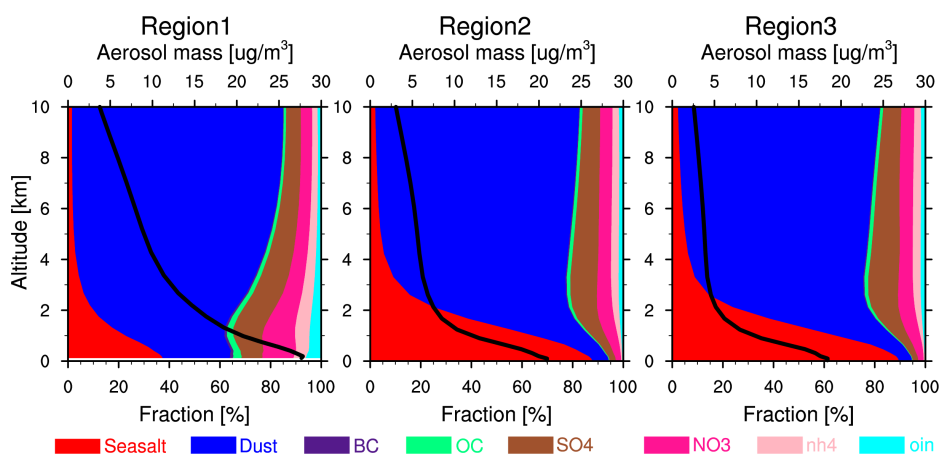
1251

Figure 12 Vertical distributions of mean aerosol mass (black solid line) and its

composition fractions (colored shade-contour) from the WRF-Chem simulations

averaged for 2010-2014 over three sub-regions as shown in Fig. 4.

1255

1256

1257

1258

1259

1260

1261

1262

1263

1264
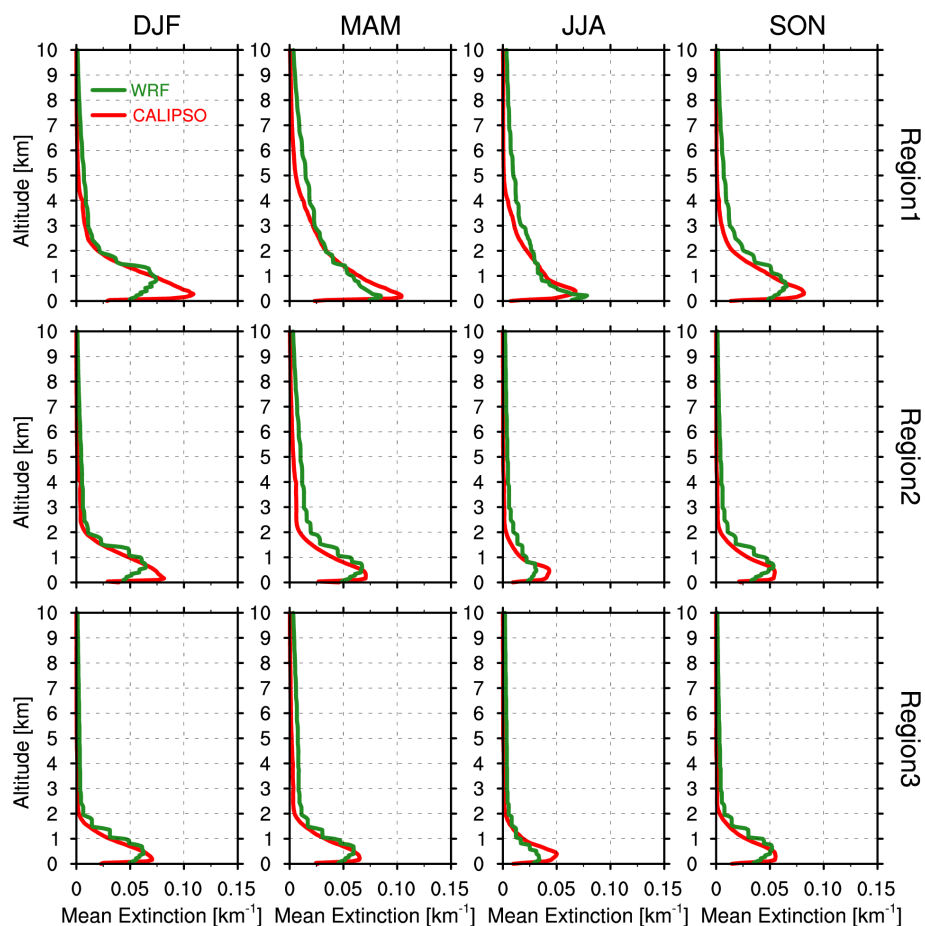
1265

Figure 13 Vertical distributions of seasonal mean aerosol extinction from the CALIPSO

retrievals and the corresponding WRF-Chem simulations averaged for 2010-2014 over

three sub-regions as shown in Fig. 4.

1269

1270

1271

1272

1273
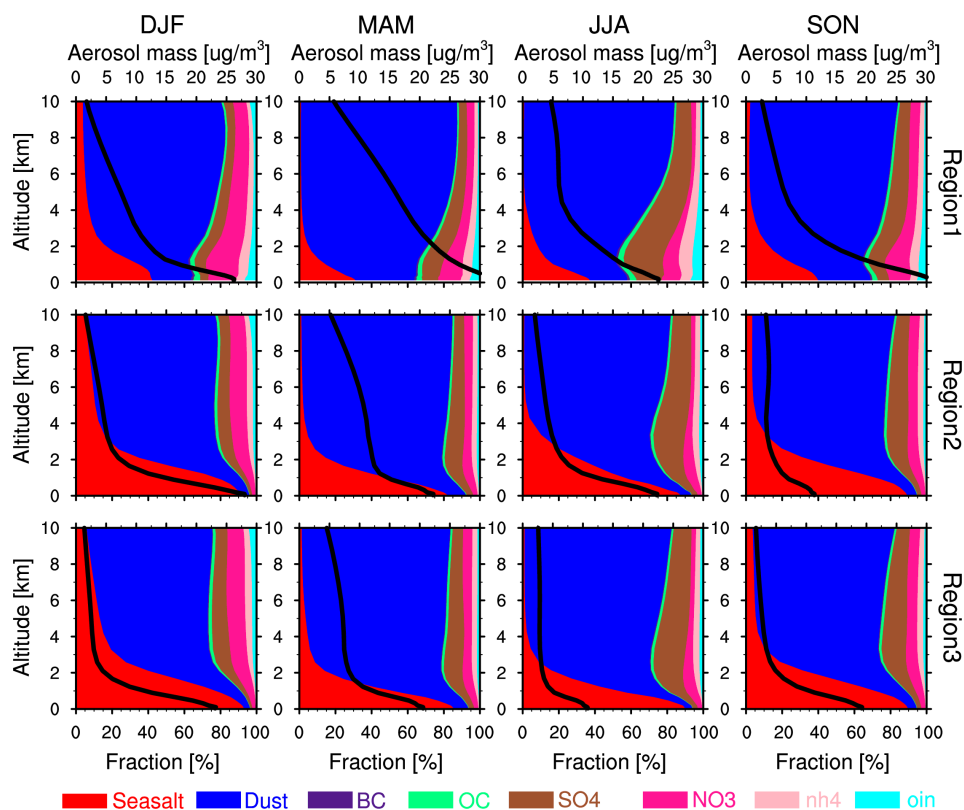
1274

Figure 14 Vertical distributions of seasonal mean aerosol mass (black solid line) and its

composition fraction (colored shade-contour) from the WRF-Chem simulations averaged

for 2010-2014 over three sub-regions as shown in Fig. 4.

1278

1279

1280

1281

1282

1283

1284
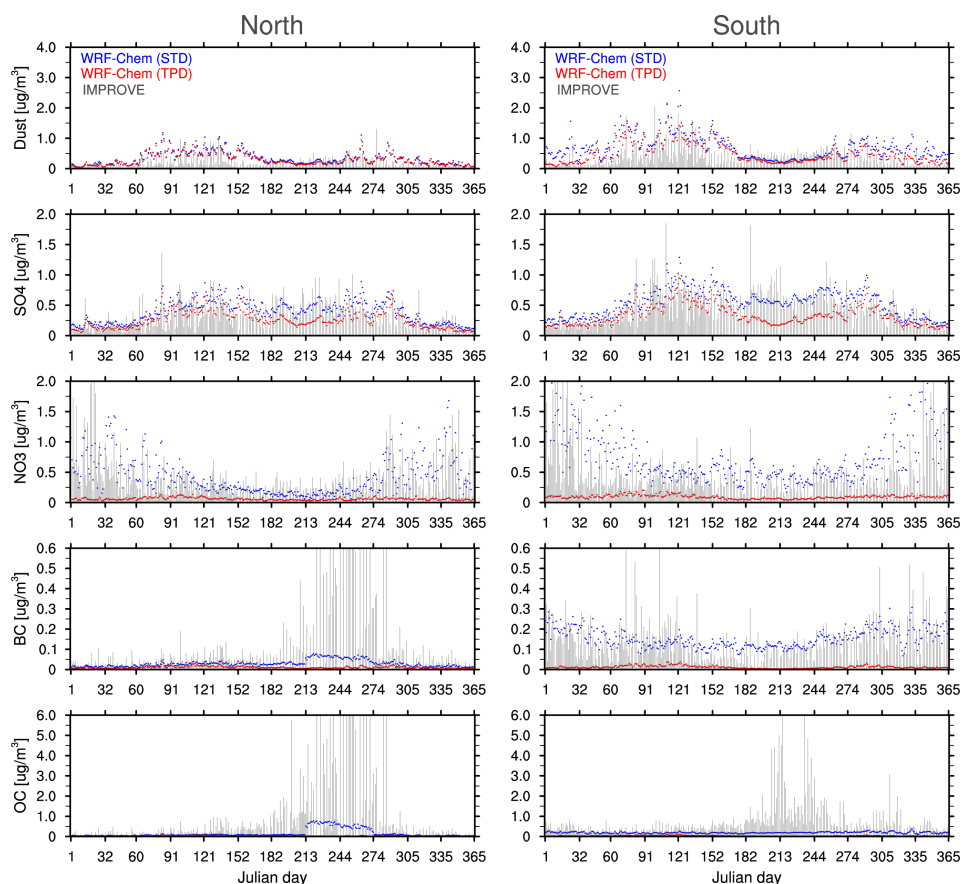
1285

1286 **Figure 15** Daily mass concentrations of fine-mode ($PM_{2.5}$) dust, sulfate, nitrate, BC, and

1287 OC averaged for 2010-2014 at the IMPROVE sites over the Northwest and Southwest

1288 US (shown in Fig. 1) from the IMPROVE observations (vertical gray bars) and the

1289 corresponding WRF-Chem standard simulations (STD; blue dots) and the sensitivity

1290 simulations without North American emissions (TPD; red dots).

1291